Theses and Dissertations

Spring 2009

Segmentations of the intraretinal surfaces, optic disc and retinal blood vessels in 3D-OCT scans

Kyung Moo Lee
University of Iowa

Recommended Citation

Lee, Kyung Moo. "Segmentations of the intraretinal surfaces, optic disc and retinal blood vessels in 3D-OCT scans." PhD (Doctor of Philosophy) thesis, University of Iowa, 2009.
http://ir.uiowa.edu/etd/247.

SEGMENTATIONS OF THE INTRARETINAL SURFACES, OPTIC DISC AND

RETINAL BLOOD VESSELS IN 3D-OCT SCANS

by

Kyung Moo Lee

An Abstract

Of a thesis submitted in partial fulfillment of the
requirements for the Doctor of Philosophy degree
in Biomedical Engineering
in the Graduate College of
The University of Iowa

May 2009

Thesis Supervisors: Professor Milan Sonka
　　　　　　　　　　Associate Professor Michael D. Abràmoff

ABSTRACT

Optical coherence tomography (OCT) is a safe and non-invasive imaging technique providing high axial resolution. A spectral-domain OCT scanner capable of acquiring volumetric data of the retina is becoming an increasingly important modality in ophthalmology for the diagnosis and management of a variety of retinal diseases such as glaucoma, diabetic retinopathy and age related macular degeneration (AMD) which are major causes of a loss of vision. To analyze and track these ocular diseases, developments of the automated methods for detecting intraretinal layers, optic discs and retinal blood vessels from spectral-domain OCT scans are highly required recently.

The major contributions of this thesis include: 1) developing a fast method that can automatically segment ten intraretinal layers in the spectral-domain macular OCT scan for the layer thickness analysis, 2) developing a method that can automatically segment the optic disc cup and neuroretinal rim in the spectral-domain OCT scan centered at the optic nerve head (ONH) to measure the cup-to-disc ratio, an important structural indicator for the progression of glaucoma, and 3) developing a method that can automatically segment the 3-D retinal blood vessels in the spectral-domain ONH-centered OCT scan to extract 3-D features of the vessels for the diagnosis of retinal vascular diseases.

Abstract Approved: _____

Thesis Supervisor

_____

Title and Department

_____

Date

_____

Thesis Supervisor

_____

Title and Department

_____

Date

SEGMENTATIONS OF THE INTRARETINAL SURFACES, OPTIC DISC AND

RETINAL BLOOD VESSELS IN 3D-OCT SCANS

by

Kyung Moo Lee

A thesis submitted in partial fulfillment of the
requirements for the Doctor of Philosophy degree
in Biomedical Engineering
in the Graduate College of
The University of Iowa

May 2009

Thesis Supervisors: Professor Milan Sonka
                    Associate Professor Michael D. Abràmoff

Graduate College
The University of Iowa
Iowa City, Iowa

CERTIFICATE OF APPROVAL

_____

PH.D. THESIS

_____

This is to certify that the Ph.D. thesis of

Kyung Moo Lee

has been approved by the Examining Committee for the thesis requirement for the
Doctor of Philosophy degree in Biomedical Engineering at the May 2009 graduation.

Thesis Committee: _____
                  Milan Sonka, Thesis Supervisor

                  _____
                  Michael D. Abràmoff, Thesis Supervisor

                  _____
                  Joseph M. Reinhardt

                  _____
                  Edwin L. Dove

                  _____
                  Michael A. Mackey

TABLE OF CONTENTS

LIST OF TABLES

LIST OF FIGURES

CHAPTER 1
INTRODUCTION

Optical coherence tomography (OCT) is a safe and non-invasive imaging technique providing high axial resolution. OCT scanners are becoming increasingly important modalities in especially ophthalmology. Unlike the time-domain OCT scanner, the spectral-domain OCT scanner recently introduced can acquire volumetric data of the retina. The OCT scanners are being used to diagnose and manage a variety of retinal diseases such as glaucoma, diabetic retinopathy and age related macular degeneration (AMD) which are major causes of a loss of vision [33]. For example, the thickness variation of a retinal nerve fiber layer (RNFL) is an important indicator to represent glaucomatous changes [16]. The ratio of the optic disc cup and rim surfaces (cup-to-disc ratio) in the spectral-domain OCT scan can also be used to determine the progression of glaucoma [1]. For another example, 3-D parameters of the retinal blood vessels may play a role in diabetic retinopathy assessment [32, 43]. Developments of the automated methods for detecting the RNFL, optic disc and retinal blood vessels from spectral-domain OCT scans are of paramount importance to help analyze, diagnose and manage these ocular diseases.

1.1   Specific aims

In particular, the specific aims for this thesis are as follows:

- **Aim 1:** Develop and validate a fast method that can automatically segment eleven retinal surfaces for ten intraretinal layers in the spectral-domain macular OCT scan.

- **Aim 2:** Develop and validate a shape-preserving method that can automatically segment the optic disc cup and neuroretinal rim in the spectral-domain OCT scan centered at the optic nerve head (ONH).

- **Aim 3:** Develop and validate a method that can automatically segment the

3-D retinal blood vessels in the spectral-domain ONH-centered OCT scan.

1.2 Thesis overview

This thesis consists of seven chapters as follows:

- Chapter 2 provides background, including intraretinal layers, retinal diseases, OCT imaging and a 3-D graph search method. In addition, it includes prior approaches and motivations for the segmentations of the intraretinal layers, optic discs and retinal blood vessels in spectral-domain OCT scans.

- Chapter 3 provides the methods and validation for the segmentation of the intraretinal layers in spectral-domain macular OCT scans.

- Chapter 4 provides the methods and validation for the segmentation of the optic discs in spectral-domain ONH-centered OCT scans

- Chapter 5 provides the methods and validation for the segmentation of the 3-D retinal blood vessels in spectral-domain ONH-centered OCT scans.

- Chapter 6 provides a general discussion and future directions.

- Chapter 7 provides the conclusions of this thesis.

CHAPTER 2
BACKGROUND AND SIGNIFICANCE

2.1   Intraretinal layers

The retina is a light sensitive part consisting of several layers at the back of the eye (Fig. 2.1). The intraretinal layers include internal limiting membrane (ILM)/nerve fiber layer (NFL), ganglion cell layer (GCL), inner plexiform layer (IPL), inner nuclear layer (INL), outer plexiform layer (OPL), outer nuclear layer (ONL), outer limiting membrane (OLM), inner segment layer (ISL), connecting cilia (CL), outer segment layer (OSL), Verhoeff's membrane (VM), retinal pigment epithelium (RPE)/Bruch's membrane (BM) and other layers (Fig. 2.2) [4].

Light comes in through the inner layers [25, 41]. The rods and cones in the ISL and OSL and their cell bodies in the ONL form the photoreceptors to convert a light signal into a neural signal. The rods are responsible for low-light black-and-white vision and distributed throughout the retina except the fovea and blind spot [21]. Rod density is greater in the peripheral retina than in the central retina. The cones are responsible for color vision. There are three types of cones, maximally sensitive to long-wavelength, medium-wavelength and short-wavelength light which are often referred to as red, green, and blue, respectively. The cones are mostly concentrated around the fovea. In the OPL, photoreceptor axons contact the dendrites of bipolar cells and horizontal cells which are interneurons aiding in signal processing. The bipolar cells in the INL transmit the neural signal from the photoreceptors and horizontal cells to their axons. In the IPL, bipolar axons contact ganglion cell dendrites and amacrine cells, another class of interneurons. The ganglion cells in the GCL transmit the neural signal through the optic nerve to the brain.
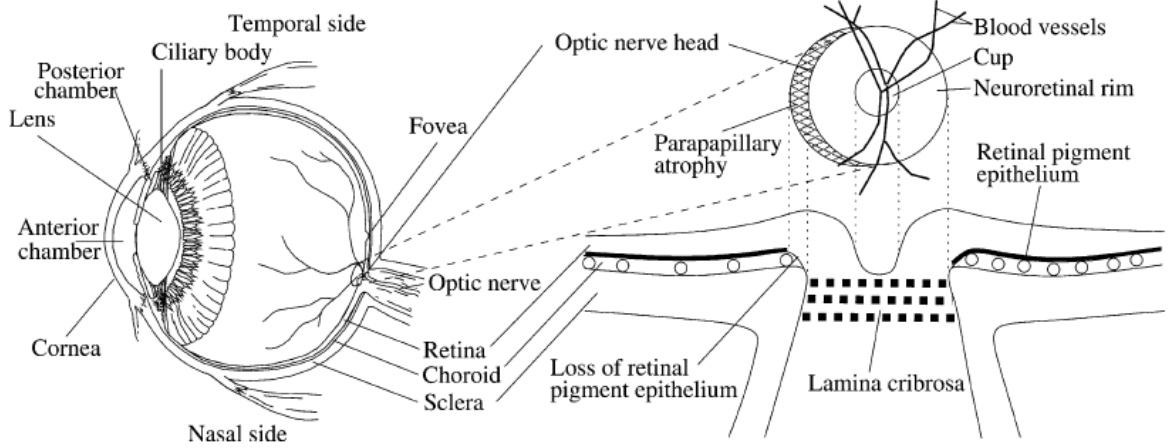
Figure 2.1: Anatomy of the eye and optic nerve head. (copied with permission from [9])

2.2 Retinal diseases

2.2.1 Glaucoma

Glaucoma is the second leading cause of blindness worldwide [37]. It is characterized by gradual cupping of the optic nerve and visual field loss [42]. An optic nerve head (ONH) is the location connecting the optic nerve and retina (Fig. 2.1). An optic disc, the 2-D structure of the ONH, consists of an optic disc cup and neuroretinal rim. The optic cup is the excavation of nerve fibers in the center, and the neuroretinal rim is formed by nerve fibers and glial cells. Glaucomatous changes in the ONH are related to a decreased number of the nerve fibers. While the size of the optic cup increases, that of the neuroretinal rim decreases (Fig. 2.3) [9]. The ratio of the optic cup and neuroretinal rim surfaces (cup-to-disc ratio) is an important structural indicator for assessing the presence of glaucoma. To quantify this ratio, planimetry has been commonly performed by glaucoma specialists from stereo color photographs [26]. Fig. 2.4(b) shows a simulated view which a glaucoma patient might see.
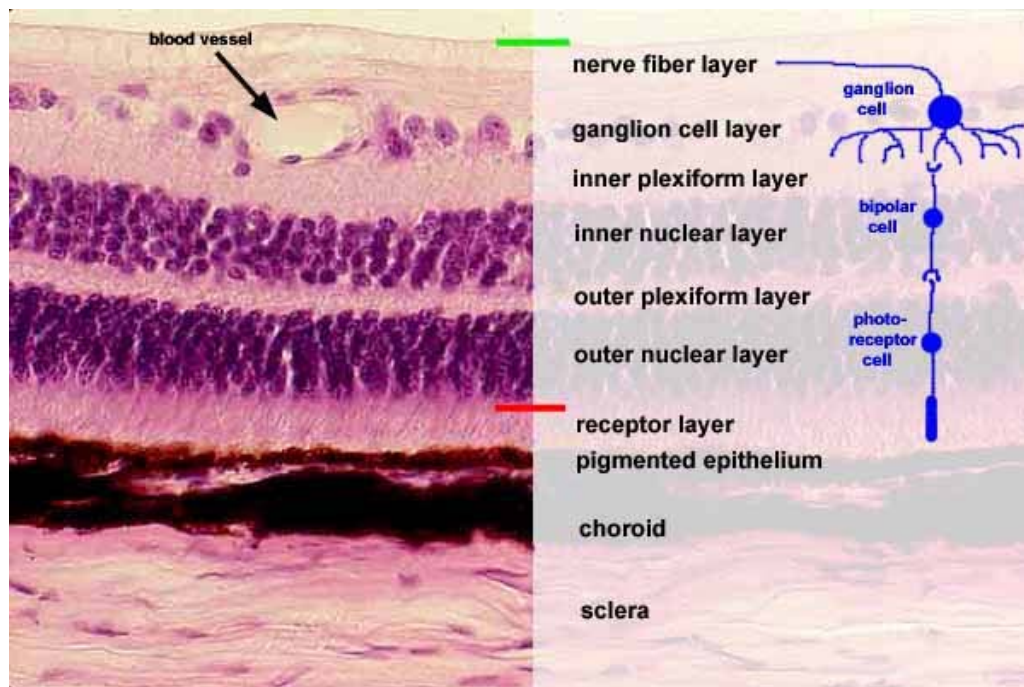
(a)
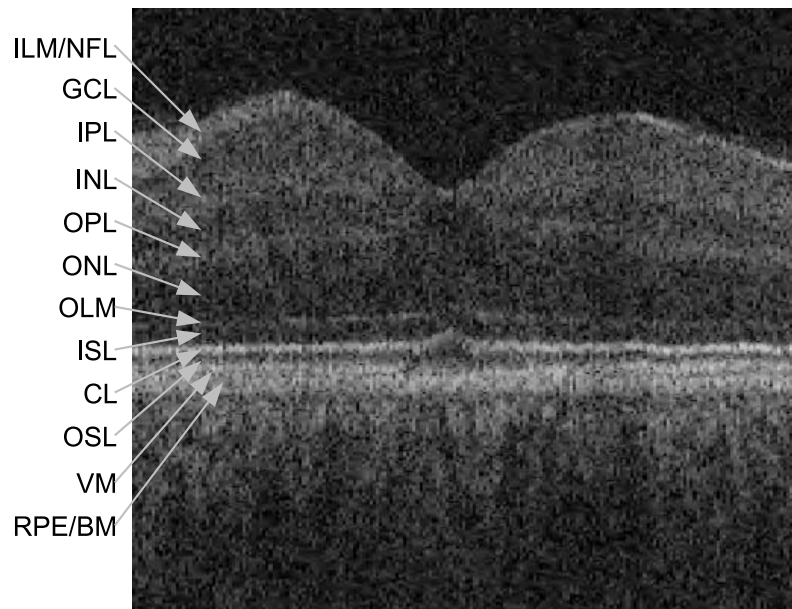
(b)

Figure 2.2: Intraretinal layers. (a) Histology. (Image courtesy of School of Medicine, The Southern Illinois University.) (b) Cross-sectional image (X-Z image) of the spectral-domain macular OCT scan around the fovea. Each intraretinal layer is distinguished by voxel intensity differences from top to bottom of the OCT scan. Light enters from the top of the image.
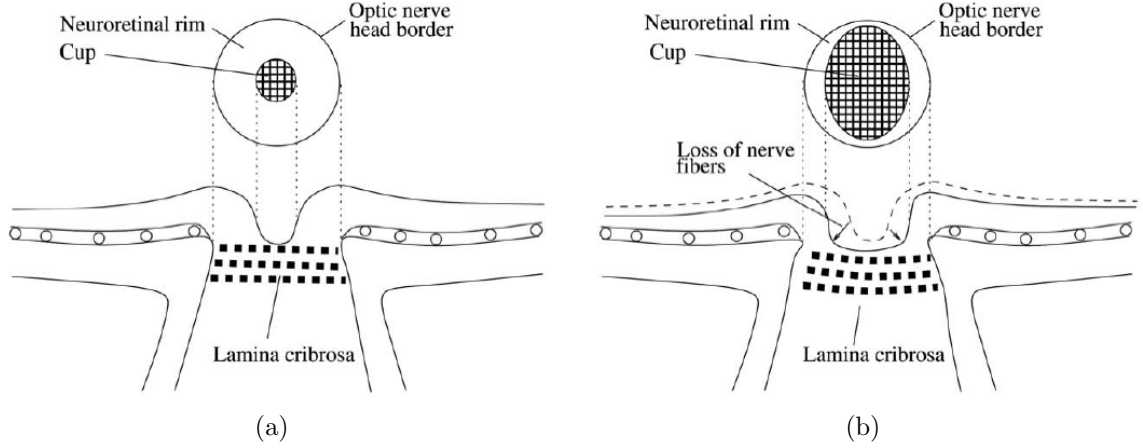
Figure 2.3: Glaucomatous changes of the ONH. (a) Normal ONH. (b) ONH with glaucomatous changes. (copied with permission from [9])

2.2.2 Diabetic retinopathy

Diabetic retinopathy is the damage to the retina caused by complications of diabetes mellitus, and the second most common cause of blindness and visual loss in the United States [24]. The blindness and visual loss can be prevented by annual screening and early diagnosis. The primary cause of the visual loss is diabetic macular edema (DME) which is a breakdown of the blood-retinal barrier due to leakage of dilated hyperpermeable capillaries and microaneurysms (Fig. 2.5) [12]. Visual deterioration is related to the degree of the DME, and the visual loss occurs when the macular edema involves the visual center. Fig. 2.4(c) shows a simulated view which a diabetic retinopathy patient might see. It is obvious that the DME affects macular structure in both short and long term.

2.3 Optical coherence tomography

2.3.1 Time-domain optical coherence tomography

Time-domain optical coherence tomography (OCT) was introduced by several groups in the early 1990s [8,15,23,38]. Fig. 2.6(a) shows a diagram about the imaging

(a)

(b)

(c)

Figure 2.4: Simulated views. (a) Normal view. (b) View of a glaucoma patient. (c) View of a diabetic retinopathy patient. (Images courtesy of National Eye Institute, National Institutes of Health.)
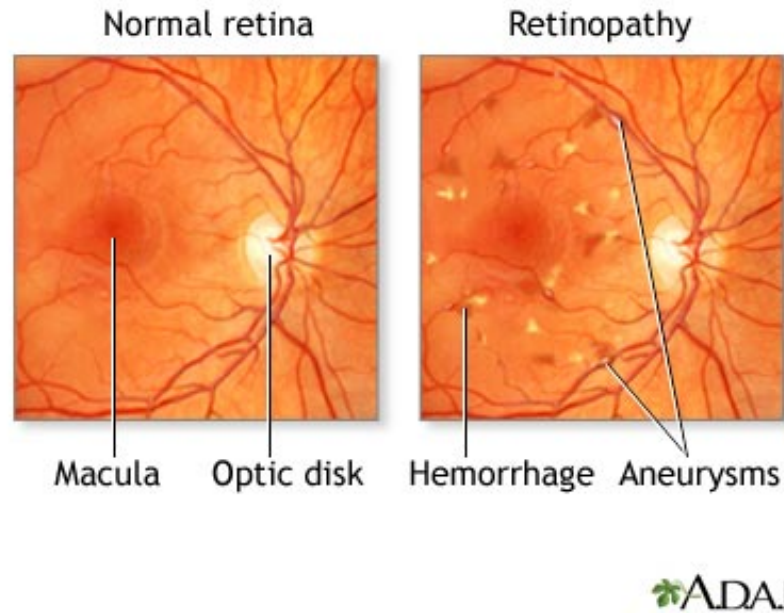
Figure 2.5: Color fundus photographs of the normal retina and abnormal retina in diabetic retinopathy [43].
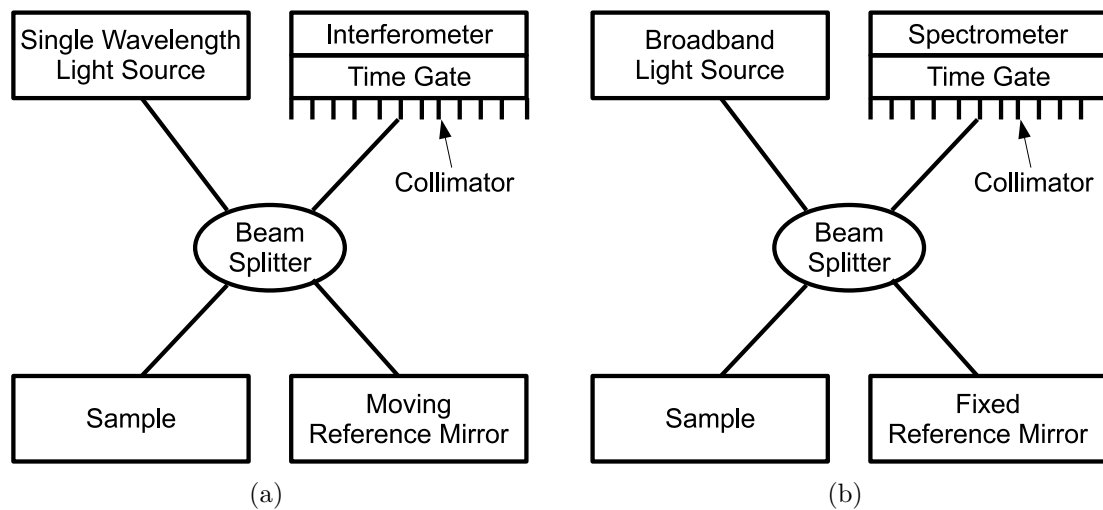
Figure 2.6: Diagrams of time-domain OCT and spectral-domain OCT systems. (a) Time-domain OCT. (b) Spectral-domain OCT.

principle of the time-domain OCT. Single wavelength light in the time-domain OCT system is splitted into the arm including a sample (i.e. retina) to be tested and the arm including a moving reference mirror. The combination of reflected lights from the sample and reference mirror causes an interference pattern when both arms have travelled in the same or similar optical distance. The envelop of the interference pattern changes depending on pathlength difference, and the peak of this envelope represents the location of the sample, with an amplitude dependent on the reflectivity of the sample. The amplitude forms a pixel or voxel intensity at the location of the sample. The interfered light is acquired by the interferometer including a time gate and collimator. A small portion of the light that reflects from the sample is collected since most light is not reflected but scattered. The scattered light has lost its original direction and does not contribute to forming an image. The time gate and collimator are used to filter out the scattered light. Although using the time gate and collimator, scattered light is detected which causes speckle noise in OCT images.

A depth scan (A-scan) is obtained by adjusting the reference mirror, and the profile of the interfered light is imaged. A cross-sectional image (B-scan) is achieved by laterally combining a series of A-scans.

The imaging principle of the time-domain OCT is analogous to that of ultrasound except the source. While the time-domain OCT system uses light, the ultrasound system uses sound. Although the imaging depth of the OCT system is shallow (around 2 mm) compared with the ultrasound system, it provides much higher axial resolution of a few microns.

The scan speed of the time-domain OCT scanner such as a Stratus OCT (Carl Zeiss Meditec, Inc., Dublin, CA, USA) machine is 400 A-scans/sec. The scan speed is limited by the speed at which the reference mirror can be moved. Therefore, the time-domain OCT scanner can acquire only several cross-sectional images (typically $6 \times 128 \times 1024$ voxels). The slow scan speed causes a bad effect on image quality
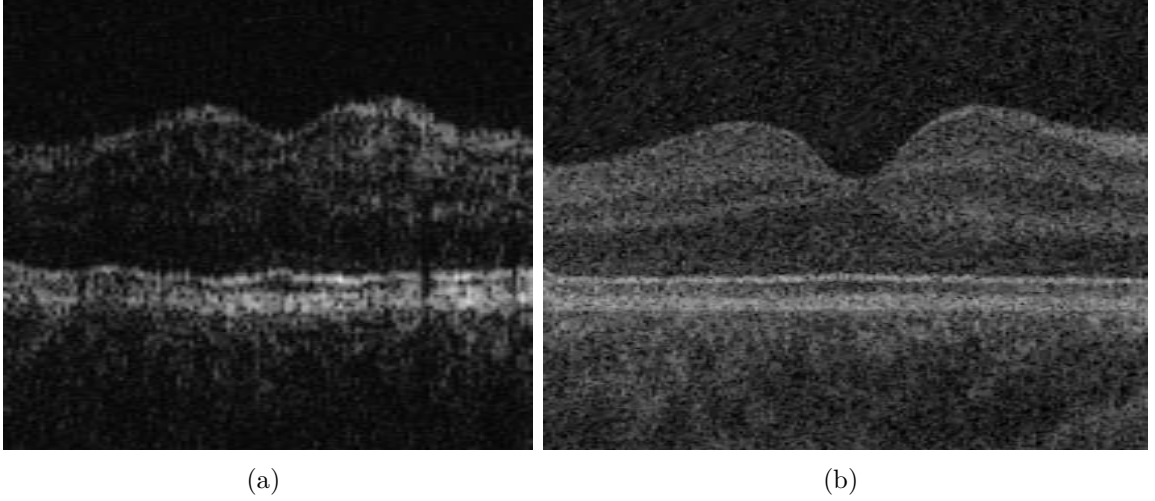
Figure 2.7: Image quality of time-domain and spectral-domain OCTs. (a) Time-domain OCT image from Stratus OCT (Carl Zeiss Meditec, Inc., Dublin, CA, USA). (b) Spectral-domain OCT image from Cirrus HD-OCT (Carl Zeiss Meditec, Inc., Dublin, CA, USA).

such as eye movement artifacts (Fig. 2.7(a)). The voxel size is $30 \times 30 \times 2 \ \mu$m, the voxel depth is 8 bits in grayscale, and the acquisition time for each scan consisting of $6 \times 128 \times 1024$ voxels is 1.92 seconds.

2.3.2 Spectral-domain optical coherence tomography

With the introduction of spectral-domain OCT scanners [14,38], imaging of the 3-D structure is now possible. Fig. 2.6(b) shows a diagram about the imaging principle of the spectral-domain OCT. The spectral-domain OCT system uses a broadband source whose center wavelength is between 800 and 1000 nm [13]. The light interfered from the tested sample and reference mirror is acquired in parallel by a spectrometer. An A-scan can be calculated by a Fourier transform from the spectrum of the acquired light.

The scan speed of the spectral-domain OCT scanner such as a Cirrus HD-OCT (Carl Zeiss Meditec, Inc., Dublin, CA, USA) machine is 27,000 A-scans/sec. The Cirrus HD-OCT scanner can acquire a retinal volume whose dimension is typically

$200 \times 200 \times 1024$ voxels covering $6 \times 6 \times 2$ mm^3. The voxel size is $30 \times 30 \times 2$ μm, the voxel depth is 8 bits in grayscale, and the acquisition time for each volumetric scan consisting of $200 \times 200 \times 1024$ voxels is 1.48 seconds. The image quality of the spectral-domain OCT is much better than that of the time-domain OCT (Fig. 2.7(b)).

The spectral-domain OCT scanner can provide true 3-D views of the retinal structure. Two kinds of OCT scans, the scan centered at the fovea (macular scan) related to central vision and the scan centered at the optic nerve head (ONH-centered scan) related to peripheral vision, are mainly acquired to examine patients' eyes (Fig. 2.8).

2.4   3-D graph search

Li et al. had developed a 3-D/4-D graph-based optimal surface detection method which can detect multiple interacting surfaces simultaneously [30, 45]. A weighted graph $G = (V, E)$ is composed of a node set V and an arc set E. The nodes $v \in V$ correspond to image pixels (or voxels) and arcs $< v_i, v_j > \in E$ connect the nodes v_i, v_j. Every arc $< v_i, v_j > \in E$ has a cost (or weight) which represents some measure of preference that the corresponding pixels belong to the object of interest. In a directed graph (or digraph), the arcs $< v_i, v_j >$ and $< v_j, v_i > (i \neq j)$ are different, and they have their own costs. In a directed arc $< v_i, v_j >$, v_i is a successor of v_j. A sequence of consecutive directed arcs $< v_0, v_1 >, < v_1, v_2 >, \cdots, < v_{k-1}, v_k >$ creates a directed path (or dipath) from v_0 to v_k. There are three types of arcs to connect the nodes v_i, v_j: intracolumn arc, intercolumn arc, and intersurface arc. Let's assume that $I(\mathbf{x}, \mathbf{y}, \mathbf{z})$ is a volumetric image, and $Col(x, y)$ is a node subset $\{V(x, y, z) | z \in \mathbf{z}\}$. For intracolumn arcs ($E^a$), along each column $Col(x, y)$, every node $V(x, y, z)(z > 0)$ has a directed arc to the node $V(x, y, z - 1)$. For intercolumn arcs (E^r), along the x-direction and for any $x \in \mathbf{x}$, a directed arc is constructed from each node $V(x, y, z) \in Col(x, y)$ to node $V(x + 1, y, max(0, z - \Delta_x)) \in Col(x + 1, y)$, where Δ_x is the smoothness constraint in the x-axis. For intersurface arcs (E^s), for
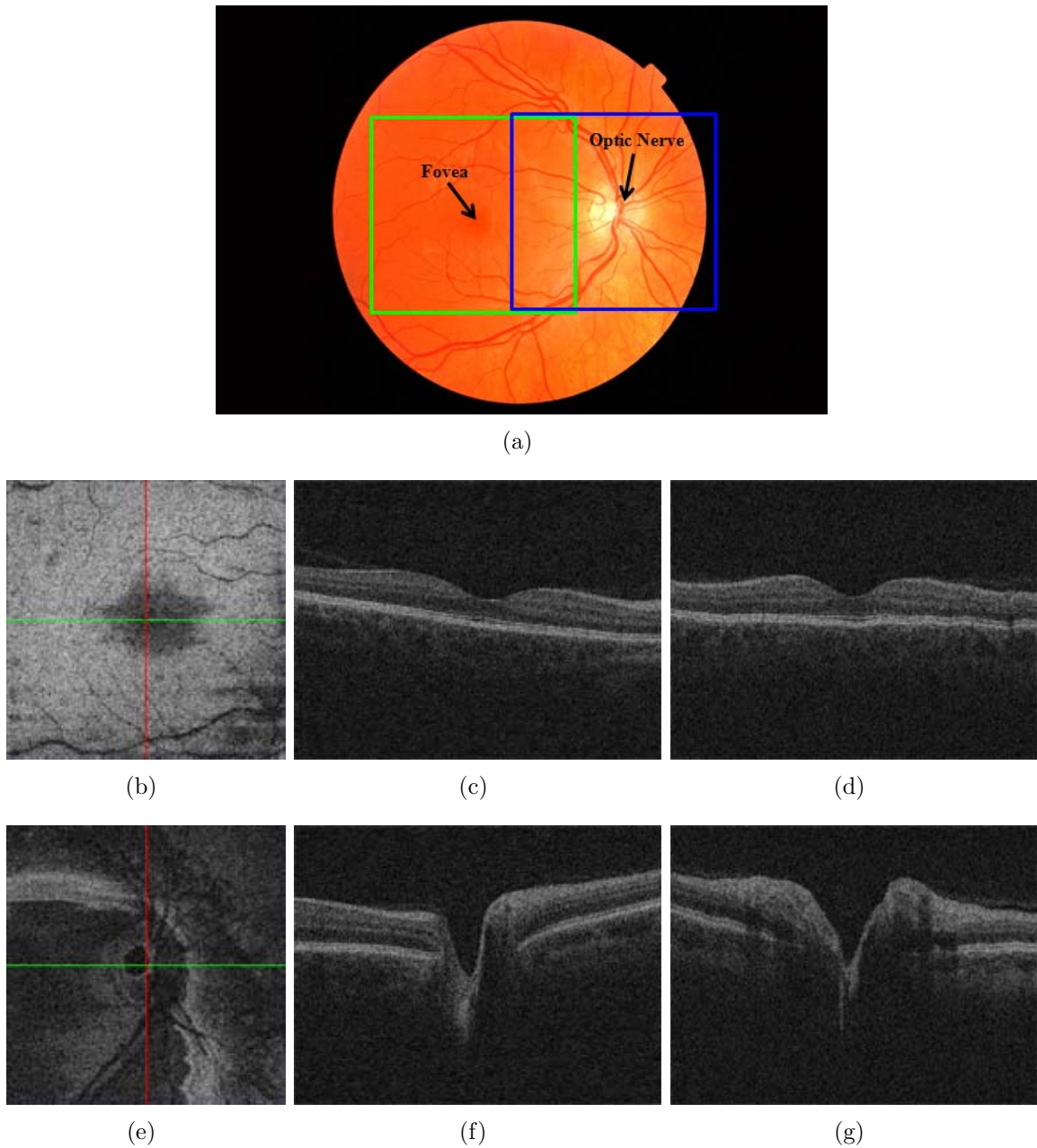
Figure 2.8: Spectral-domain volumetric OCT scans of the retina. (a) Color fundus photograph of the retina. The green square shows the position of the scan centered at the fovea (macular scan), and the blue square represents the position of the scan centered at the ONH (ONH-centered scan). (b) X-Y image of the macular scan. (c) X-Z image of the macular scan corresponding to the green line in image (b). (d) Y-Z image of the macular scan corresponding to the red line in image (b). (e) X-Y image of the ONH-centered scan. (f) X-Z image of the ONH-centered scan corresponding to the green line in image (e). (g) Y-Z image of the ONH-centered scan corresponding to the red line in image (e).
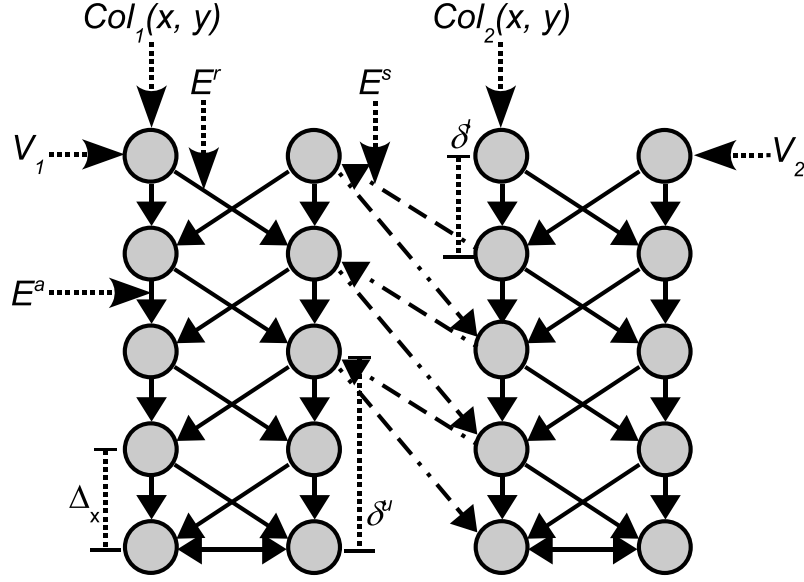
Figure 2.9: Graph construction for the detection of double surfaces.

any node $V_1(x, y, z)$ in $Col_1(x, y)$ with $z \geq \delta^u$, a directed arc connecting $V_1(x, y, z)$ to $V_2(x, y, z - \delta^u)$ is constructed. Also, for each node $V_2(x, y, z)$ in $Col_2(x, y)$ with $z < Z - \delta^l$, a directed arc connecting $V_2(x, y, z)$ to $V_1(x, y, z + \delta^l)$ is created. δ^u and δ^l are the maximum and minimum surface separation constraints, respectively (Figs. 2.9, 2.10). Segmentation of the optimal surfaces is formulated as computing a minimum closed set in the 3-D geometric graph constructed from cost functions. This can be solved by computing the minimum $s - t$ cut of the graph with a low-order polynomial time complexity.

2.5 Segmentation of the intraretinal layers in 3-D macular OCT scans

2.5.1 Prior approaches

Several research on intraretinal layer segmentation of both time-domain and spectral-domain macular OCT scans has been previously performed.

Fuller et al. proposed a semi-automatic segmentation method using a support vector machine (SVM) trained with OCT voxel intensities marked by a user to detect
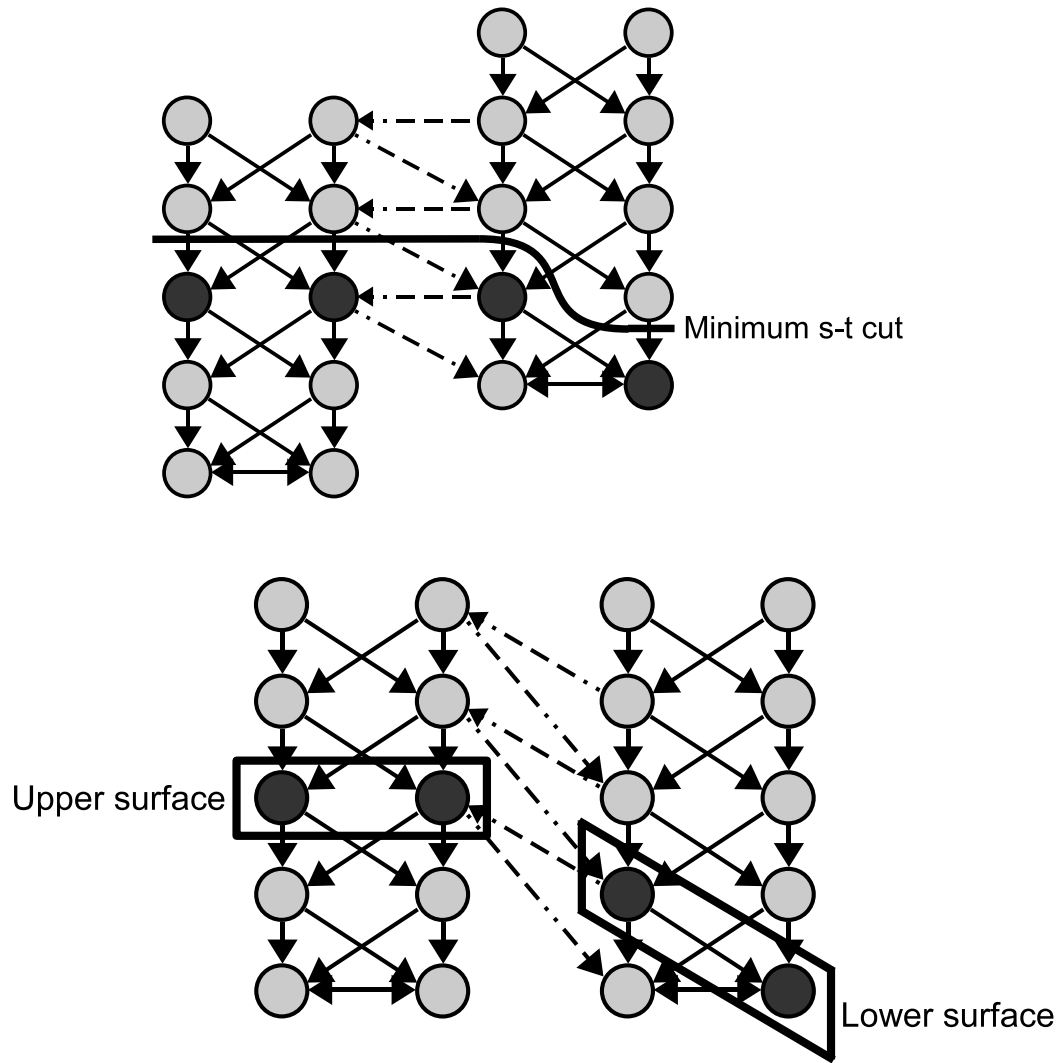
Figure 2.10: Detection of the double surfaces by computing the minimum $s - t$ cut of the graph.

2 retinal surfaces in spectral-domain macular scans [17].

Fernández et al. introduced both automatic and semi-automatic segmentation methods using texture analysis by means of the structure tensor combined with complex diffusion filtering. The automatic and semi-automatic methods detected 7 and 10 retinal boundaries in time-domain macular scans, respectively. However, the segmentation results which they showed are not visually accurate around the fovea, and they did not represent quantitative segmentation errors [16].

Garvin detected 7 retinal surfaces in spectral-domain macular scans using a 3-D graph search approach with the incorporation of regional information and varying constraints. Although her method can detect optimal retinal surfaces with respect to her cost functions, it requires long processing time and a large memory capacity [19, 20].

2.5.2   Motivation

Intraretinal layer segmentation is of importance to monitor the progress of retinal diseases such as the variation of the RNFL and macular edema formation. A study on the intraretinal layer segmentation method which is fast, accurate and capable of detecting more layers is highly required. Our study is directly motivated by Garvin's preliminary research [19, 20] and Gerth's paper [4].

2.6   Segmentation of the optic disc in 3-D ONH-centered OCT scans

2.6.1   Prior approaches

Previously several groups, including ours, have studied a variety of automated methods to segment and quantify the optic discs from 2-D retinal images [1, 6, 46].

Carmona et al. introduced an automatic system to locate and segment the optic disc in eye fundus images using genetic algorithms [6]. The genetic algorithm was used to find an ellipse containing the maximum number of hypothesis points. However, this method has a potential error if the shape of the optic disc is not a perfect ellipse,

and the method did not segment the optic disc cup.

Xu et al. developed an automated system for assessment of the optic disc on stereo disc photographs [46]. They used a deformable model technique, which deforms an initial contour to minimize the energy function defined from contour shape and contour location, to detect optic cup and disc margins.

Abràmoff et al. presented a study on the automated segmentation method of the optic disc cup and rim from stereo color photographs using pixel feature classification, including a depth from stereo disparity feature, and compared their segmentation results with glaucoma experts and glaucoma experts in training [1].

2.6.2   Motivation

Although direct quantification of ONH parameters in 3-D seems attractive, clinical management is historically based on assessment of the optic disc in stereo color photographs [26]. Since glaucoma is a slowly progressive disease, with changes occurring over many years, it is currently not clear what 3-D ONH parameters, if any, are suitable for glaucoma progression measurement. Therefore, in order to allow comparisons with historically accepted optic disc planimetry, segmentation of the optic disc directly from the 3-D OCT is attractive. The question whether automated planimetry can be performed directly from 3-D OCT scans is open and, to the best of our knowledge, has not been previously studied.

2.7   Segmentation of the retinal blood vessels in 3-D ONH-centered OCT scans

2.7.1   Prior approaches

Many studies on 2-D segmentation of retinal blood vessels from a variety of medical images have been performed.

Gang et al. introduced a matched filter-based method using an amplitude-modified second-order Gaussian filter to detect and measure retinal vessels in color fundus im-

ages [18].

Hoover et al. proposed a thresholding-based method to locate and outline blood vessels in ocular fundus images using a piecewise threshold obtained from local and global vessel features cooperatively [22].

Can et al. presented a tracking-based method to trace retinal vasculature in live retinal video angiograms and extract features such as intersections and crossovers [5].

Zana et al. introduced a mathematical morphology-based method using curvature evaluation to detect vessel-like patterns in noisy color fundus images [47].

Staal et al. proposed a classification-based method to segment blood vessels in color images of the retina. Image ridges coinciding approximately with vessel center-lines were used as feature vectors [40].

Xu et al. presented a hybrid algorithm using a matched filter, mathematical morphology, contrast enhancement and thresholding probe for segmentation of the retinal vessels in scanning laser ophthalmoscopy (SLO) images [46].

Niemeijer et al. proposed a supervised pixel classification-based vessel segmentation approach in OCT projection images [33].

2.7.2   Motivation

Segmentation of retinal blood vessels plays an important role in the diagnosis of retinal vascular disease including diabetic retinopathy. Several morphological features such as diameter, length, branching angle, and tortuosity of veins and arteries in the retina have diagnostic relevance [36]. Many studies on 2-D segmentation of the retinal blood vessels from a variety of medical images such as color fundus images, retinal video angiograms, SLO images and OCT projection images have been performed. However, 3-D segmentation of the retinal blood vessels in spectral-domain OCT volumes, which can provide 3-D features of the vessels for the diagnosis of retinal vascular diseases, to the best of our knowledge, has not been previously studied. Localization of the retinal vessels in 3-D including their depth in the retina has the

potential to increase our understanding of the oxygenation of the inner retina close to the optic disc. Possibly the depth distribution of the vessels in a subject, i.e. how many of their vessels are "superficial" rather than "deep" can be an independent risk for glaucoma and retinal vascular diseases. The distribution may even be genetically distributed.

CHAPTER 3
SEGMENTATION OF THE INTRARETINAL LAYERS IN 3-D MACULAR OCT SCANS

3.1   Methods

We developed a method which can detect ten intraretinal layers identified by eleven retinal surfaces in spectral-domain OCT scans. First, the retinal surfaces which will be segmented in this study were defined in Section 3.1.1. The multiscale 3-D graph search, a fast extension of the 3-D graph search method, was developed to segment these intraretinal layers [27] (Sections 3.1.2, 3.1.3 and 3.1.4). The multiscale 3-D graph search approach detects the surface in a high-resolution OCT subvolume constrained by the surface segmented at a lower resolution. Therefore, a fast processing is possible by dealing with several OCT subvolumes instead of a whole OCT volume. An edge-based cost function of the graph search, which consisted of gradient magnitudes of the dark-to-bright or bright-to-dark transition from top to bottom of the OCT volume, were used for each retinal surface.

3.1.1   Definition of eleven retinal surfaces

A retina includes many intraretinal layers such as ILM/NFL, GCL, IPL, INL, OPL, ONL, OLM, ISL, CL, OSL, VM and RPE/BM (Fig. 3.1). Each intraretinal layer is identified by two retinal surfaces which have the dark-to-bright or bright-to-dark transition of voxel intensities from top to bottom of the spectral-domain OCT scan. Fig. 3.1(b) shows the intraretinal surfaces (surfaces 1 – 11) which will be segmented in this study. While surfaces 1, 3, 5, 7, 9 and 10 have the dark-to-bright transition from top to bottom of the OCT scan, surfaces 2, 4, 6, 8 and 11 have the bright-to-dark transition. Segmentation of OLM and ISL is excluded in this study since they are obscure in spectral-domain macular OCT scans.

(a)	(b)
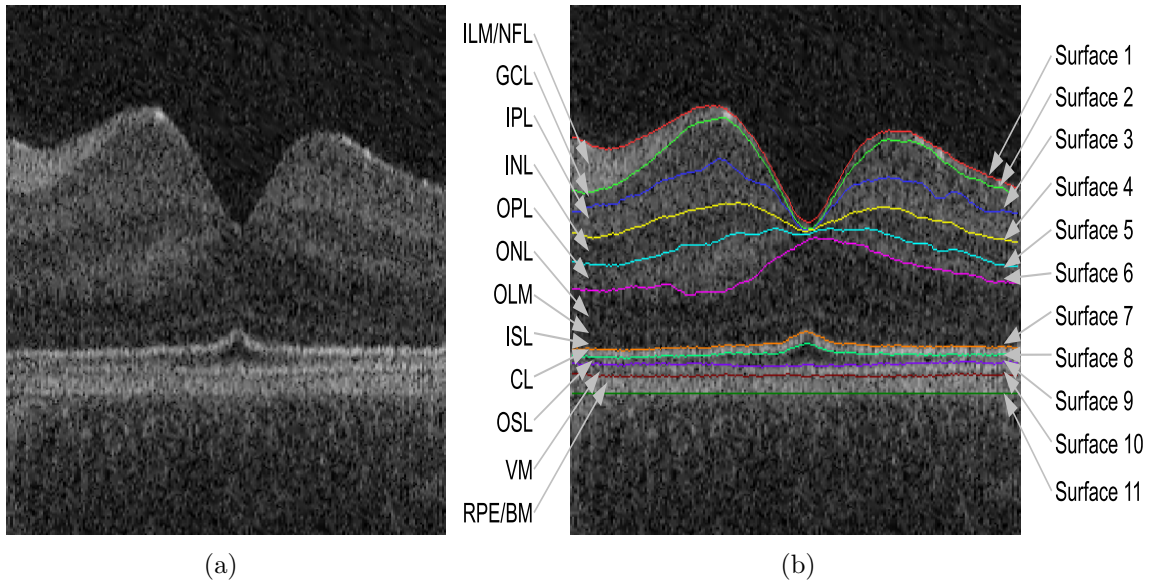
Figure 3.1: Definition of eleven retinal surfaces (surfaces 1 – 11). (a) X-Z image of the flattened macular OCT scan from a normal subject. (b) Image (a) overlapped with eleven retinal surfaces.
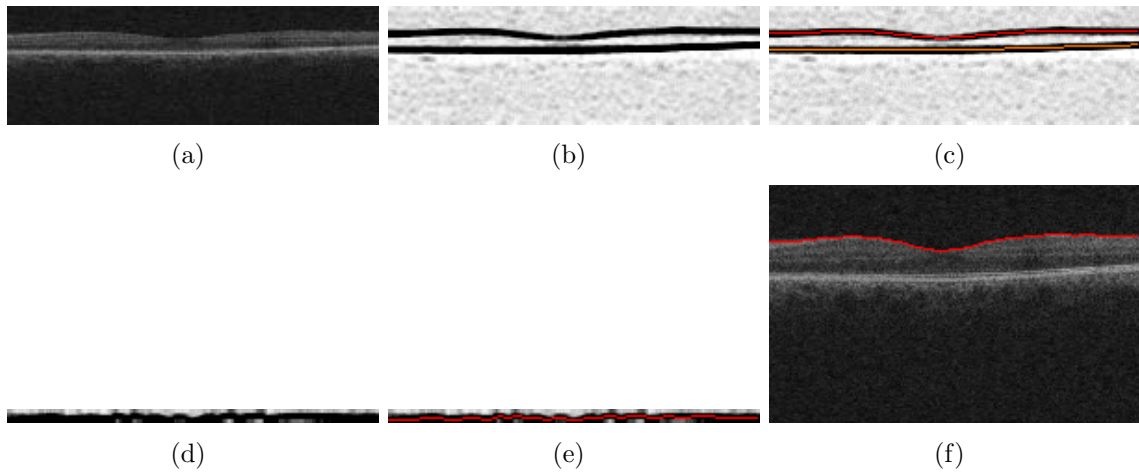
Figure 3.2: Segmentation of surfaces 1 in levels 1 and 2. (a) OCT volume in level 1. (b) Cost function in level 1. (c) Cost function in level 1 overlapped with segmented surface 1 (top line) and the surface combined of surfaces 7, 9 and 10 (bottom line). (d) Cost function of the OCT subvolume in level 2 constrained by surface 1 segmented in level 1. (e) Cost function (d) overlapped with segmented surface 1. (f) OCT volume in level 2 overlapped with segmented surface 1.

3.1.2 Segmentation of surfaces 1 and 7

Using a multiscale 3-D graph search method, surfaces 1 and 7 were detected in spectral-domain OCT scans. The method starts by creating five multiscale OCT volumes subsampled by a factor of 2 in the z-axis. Level 5 represents full resolution, and level 1 is the lowest resolution. This subsampling process has an effect on reducing speckle noise in OCT volumes of low resolutions so that some retinal surfaces have clear borders in low resolutions. Fig. 3.2(a) shows two clear surfaces, surface 1 and the surface combined of surfaces 7, 9 and 10 in the OCT volume in level 1, and they were detected using a 3-D double surface graph search method (Fig. 3.2(c)). The cost functions for the 3-D double surface graph search method were smoothed, inverted gradient magnitudes of the dark-to-bright transition from top to bottom of the OCT volume in level 1 (Fig. 3.2(b)). A $3 \times 3 \times 3$ averaging filter was used to improve the connectivity of the surfaces as well as reduce the OCT speckle noise. The smoothed gradient magnitudes were inverted since the 3-D double surface graph search method detects two optimal surfaces having the minimum cost. Surface 1 segmented in level 1 provided the approximate z-positions of surface 1 in level 2 by multiplying the z-positions of surface 1 in level 1 by 2. In the OCT subvolume, which consists of the OCT volume constrained by two surfaces having small margins in the z-axis above and below the approximate surface 1 in level 2, accurate surface 1 in level 2 was detected using a 3-D single surface graph search (Fig. 3.2(d–e)). Surface 1 segmented in the OCT subvolume is inversely transformed into the OCT volume in level 2 (Fig. 3.2(f)). In the same fashion, surfaces 1 in levels 3, 4 and finally 5 were hierarchically detected. Segmentation of surface 7 is the same as that of surface 1 except using a 3-D double surface graph search based on the surface combined of surfaces 7, 9 and 10 in the OCT volume in level 1 (the bottom line in Fig. 3.2(c)). The 3-D double surface graph search method detected two surfaces, surface 7 and the surface combined of surfaces 9 and 10. If a 3-D single surface graph search is applied
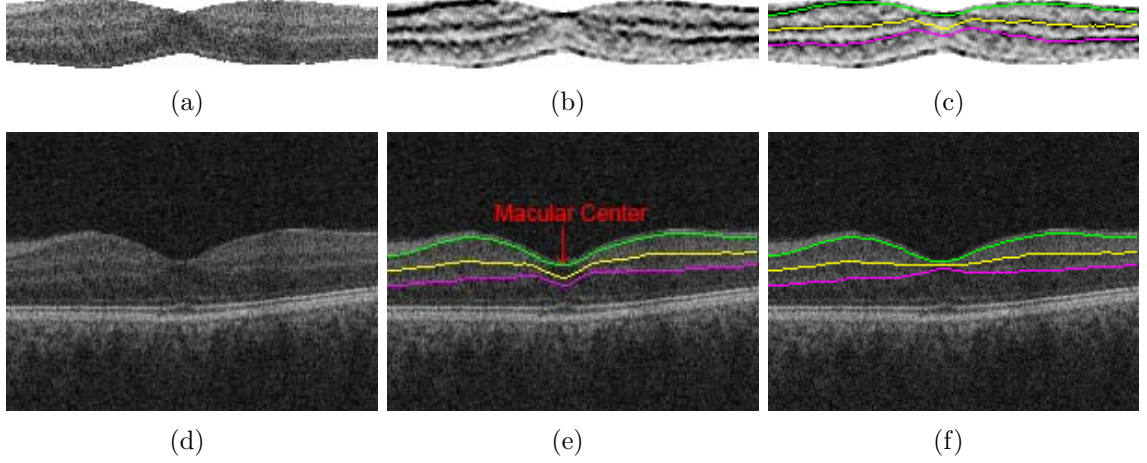
Figure 3.3: Segmentation of surfaces 2, 4 and 6 in level 3. (a) OCT subvolume in level 3. (b) Cost function. (c) Cost function overlapped with the segmented surfaces. (d) OCT volume in level 3. (e) OCT volume in level 3 overlapped with the segmented surfaces inversely transformed from image (c). (f) OCT volume in level 3 overlapped with the modified surfaces.

to segment surface 7, the segmentation result would be locally distracted by surfaces 9 and 10 since they have the same properties of the dark-to-bright transition from top to bottom of the OCT volume. Explanation about segmentation of surfaces 9 and 10 will be described in Section 3.1.4.

3.1.3   Segmentation of surfaces 2, 3, 4, 5 and 6

For segmentation of surfaces 2, 3, 4, 5 and 6, levels 3, 4, 5 was used since these surfaces are not clear in lower resolutions such as levels 1 and 2. Surfaces 2, 4 and 6 exist between segmented surfaces 1 and 7 with the bright-to-dark transition from top to bottom of the OCT volume. The OCT subvolume in level 3 between surfaces 1 and 7 was created based on the middle surface of surfaces 1 and 7 (Fig. 3.3(a)). Surfaces 2, 4 and 6 in the OCT subvolume were segmented by a 3-D triple surface graph search method using cost functions which were smoothed, inverted gradient magnitudes of the bright-to-dark transition from top to bottom of the OCT subvolume (Figs. 3.3(b–c)). Surfaces 2, 4 and 6 segmented in the OCT subvolume were inversely transformed

into the OCT volume in level 3 (Fig. 3.3(e)). Due to surface separation constraints of the 3-D triple surface graph search method, the segmentation results of surfaces 2, 4 and 6 around the macular center are not accurate. In order to solve this problem, surfaces 2, 4 and 6 around the macular center were modified using thin-plate splines which were fitted to surface 2, 4 and 6 excluding the subsurfaces around the macular center and the macular center (Fig. 3.3(f)). The macular center was positioned 3 voxels below segmented surface 1 at the (x, y) location having the minimum distance between segmented surfaces 1 and 7. Based on surfaces 2, 4 and 6 modified in level 3, surfaces 2, 4 and 6 in levels 4 and 5 were detected by hierarchically applying three 3-D single surface graph searches for each level. Surfaces 2 and 5 can be distinguished by the dark-to-bright transition from top to bottom of the OCT volume between surfaces 1 and 3 and between surfaces 4 and 6, respectively. In levels 3, 4 and 5, surfaces 2 and 5 were hierarchically segmented using two 3-D single surface graph search methods for each level.

3.1.4   Segmentation of surfaces 8, 9, 10 and 11

For segmentation of surfaces 8, 9, 10 and 11, only level 5 was utilized since they are obscure in lower resolutions. Surfaces 8 and 11 were defined by the bright-to-dark transition from top to bottom of the OCT volume below surface 7 and below the surface combined of surfaces 9 and 10 in Section 3.1.2, respectively. Surfaces 8 and 11 in level 5 were detected by applying two 3-D single surface graph searches, respectively. Surface 10 exists right above segmented surface 11 with the dark-to-bright gray transition from top to bottom of the OCT volume. Surface 10 in level 5 was detected by a 3-D single surface graph search. Finally, surface 9 exists between segmented surfaces 8 and 10 with the dark-to-gray transition from top to bottom of the OCT volume, and it was detected by a 3-D single surface graph search.

3.2 Experiments

3.2.1 Data

Fourteen spectral-domain macular OCT scans were acquired from the right eyes of 14 normal subjects at the University of Iowa using Cirrus HD-OCT (Carl Zeiss Meditec, Inc., Dublin, CA, USA) machines. Each OCT scan consists of $200 \times 200 \times 1024$ voxels covering $6 \times 6 \times 2$ mm^3, the voxel size is $30 \times 30 \times 2$ μm, and the voxel depth is 8 bits in grayscale. The acquisition time of each volumetric scan is 1.48 seconds. The Institutional Review Board of the University of Iowa approved the research protocol.

To validate our intraretinal layer segmentation method, our segmentation results were compared with reference standards which were created by averaging in the z-direction manual tracings obtained from two ophthalmologists. The manual tracings were performed in 10 randomly selected X-Z images for each volumetric OCT scan so 140 X-Z images from 14 OCT scans were used for validation.

3.2.2 Validation

To evaluate our intraretinal layer segmentation approach, our segmentation results were compared with the reference standards. The accuracy of our segmentation results was estimated by unsigned/signed border positioning errors and absolute layer thickness differences. The unsigned/signed border positioning errors were calculated by measuring unsigned/signed Euclidean distances in the z-axis between our segmentation results and the reference standards, respectively. If our segmentation result is located above the reference standard, the signed border positioning error is negative, otherwise positive. To validate the method, the unsigned/signed border positioning errors were compared with the unsigned/signed border positioning differences between two manual tracings. If the manual tracing from observer 2 is located above that from observer 1, the signed border positioning difference is negative, otherwise

Table 3.1: Mean unsigned border positioning errors between our segmentation results and reference standards, and mean unsigned border positioning differences between manual tracings from two observers (Mean ± SD).

Surface	Algo. vs. Ref. (voxel)	Algo. vs. Ref. (μm)	Obs. 1 vs. Obs. 2 (voxel)	Obs. 1 vs. Obs. 2 (μm)
1	1.35 ± 1.08	2.70 ± 2.15	1.83 ± 1.46	3.65 ± 2.92
2	3.45 ± 4.29	6.89 ± 8.59	6.99 ± 7.67	13.99 ± 15.35
3	6.80 ± 5.19	13.59 ± 10.38	16.94 ± 7.80	33.89 ± 15.59
4	2.49 ± 2.47	4.98 ± 4.93	3.63 ± 3.54	7.27 ± 7.08
5	3.72 ± 2.61	7.45 ± 5.21	3.75 ± 3.64	7.50 ± 7.29
6	2.94 ± 2.56	5.87 ± 5.13	3.29 ± 2.94	6.58 ± 5.89
7	1.57 ± 2.61	3.13 ± 5.21	2.44 ± 5.26	4.87 ± 10.51
8	1.30 ± 1.21	2.59 ± 2.42	1.97 ± 2.03	3.95 ± 4.05
9	2.69 ± 1.93	5.37 ± 3.87	3.70 ± 2.71	7.40 ± 5.41
10	3.30 ± 2.44	6.60 ± 4.88	3.32 ± 2.50	6.63 ± 5.00
11	2.03 ± 1.69	4.07 ± 3.39	2.44 ± 2.17	4.88 ± 4.34
overall	2.88 ± 2.55	5.75 ± 5.11	4.57 ± 3.79	9.15 ± 7.58

positive. In addition, the absolute thickness differences between our segmentation results and the reference standards were compared with those between two manual tracings. After confirming the normal distributions of two datasets by the Shapiro-Wilk test, a paired t-test was used in the 95% confidence interval to compare these two datasets.

3.3   Results

Table 3.1 shows mean unsigned border positioning errors between our segmentation results and the reference standards, and mean unsigned border positioning differences between manual tracings from two observers. Table 3.2 represents p-values for paired t-tests between the mean unsigned border positioning errors and differences. While the unsigned border positioning errors of surfaces 1, 2, 3, 4, 6, 7, 8, 9 and 11 were significantly smaller than the unsigned border positioning differences, those of surfaces 5 and 10 were not significantly different from the unsigned border positioning differences.

Table 3.2: p-values for paired t-tests between unsigned border positioning errors between our segmentation results and the reference standards, and unsigned border positioning differences between manual tracings from two observers.

Surface	p-value
1	< 0.01
2	< 0.01
3	< 0.01
4	< 0.01
5	> 0.21
6	< 0.01
7	< 0.01
8	< 0.01
9	< 0.01
10	> 0.40
11	< 0.01

Table 3.3: Mean signed border positioning errors between our segmentation results and reference standards, and mean signed border positioning differences between manual tracings from two observers (Mean $\pm$ SD).

Surface	Algo. vs. Ref. (voxel)	Algo. vs. Ref. (μm)	Obs. 1 vs. Obs. 2 (voxel)	Obs. 1 vs. Obs. 2 (μm)
1	-0.62 ± 1.61	-1.24 ± 3.22	0.07 ± 2.34	0.14 ± 4.68
2	2.18 ± 5.06	4.35 ± 10.11	6.23 ± 8.31	12.45 ± 16.62
3	6.33 ± 5.76	12.65 ± 11.51	16.88 ± 7.93	33.77 ± 15.85
4	-0.36 ± 3.49	-0.71 ± 6.98	-0.35 ± 5.06	-0.70 ± 10.12
5	-3.22 ± 3.20	-6.44 ± 6.41	1.65 ± 4.96	3.30 ± 9.93
6	-2.09 ± 3.29	-4.19 ± 6.58	0.93 ± 4.32	1.86 ± 8.63
7	-0.37 ± 3.02	-0.74 ± 6.04	0.53 ± 5.77	1.06 ± 11.54
8	0.44 ± 1.72	0.89 ± 3.43	0.45 ± 2.79	0.90 ± 5.59
9	-0.34 ± 3.29	-0.68 ± 6.58	2.25 ± 3.99	4.49 ± 7.99
10	-2.74 ± 3.06	-5.47 ± 6.11	-0.22 ± 4.15	-0.43 ± 8.29
11	0.91 ± 2.48	1.82 ± 4.97	0.14 ± 3.26	0.29 ± 6.53

Table 3.4: p-values for paired t-tests between signed border positioning errors between our segmentation results and reference standards, and signed border positioning differences between manual tracings from two observers.

Surface	p-value
1	< 0.01
2	< 0.01
3	< 0.01
4	> 0.90
5	< 0.01
6	< 0.01
7	< 0.01
8	> 0.81
9	< 0.01
10	< 0.01
11	< 0.01

Table 3.3 shows mean signed border positioning errors between our segmentation results and the reference standards, and mean signed border positioning differences between manual tracings from two observers. Table 3.4 represents p-values for paired t-tests between the mean signed border positioning errors and differences. While the signed border positioning errors of surfaces 2, 3, 7 and 9 were significantly smaller than the signed border positioning differences, those of surfaces 1, 5, 6, 10 and 11 were significantly larger than the signed border positioning differences. There were no significant differences in surfaces 4 and 8. Additionally while our segmentation results were located slightly above the reference standards in surfaces 1, 4, 5, 6, 7, 9 and 10, those were not in the remaining surfaces.

Table 3.5 shows mean absolute thicknesses differences between our segmentation results and the reference standards, and between manual tracings from two observers. In all layers except layer 10-11, absolute thicknesses differences between our segmentation results and the reference standards were significantly smaller than those between manual tracings from two observers.

Figs. 3.4 and 3.5 show our segmentation results in the best and worst performance

(a) Slice 16

(b) Slice 24

(c) Slice 62

(d) Slice 83

(e) Slice 93
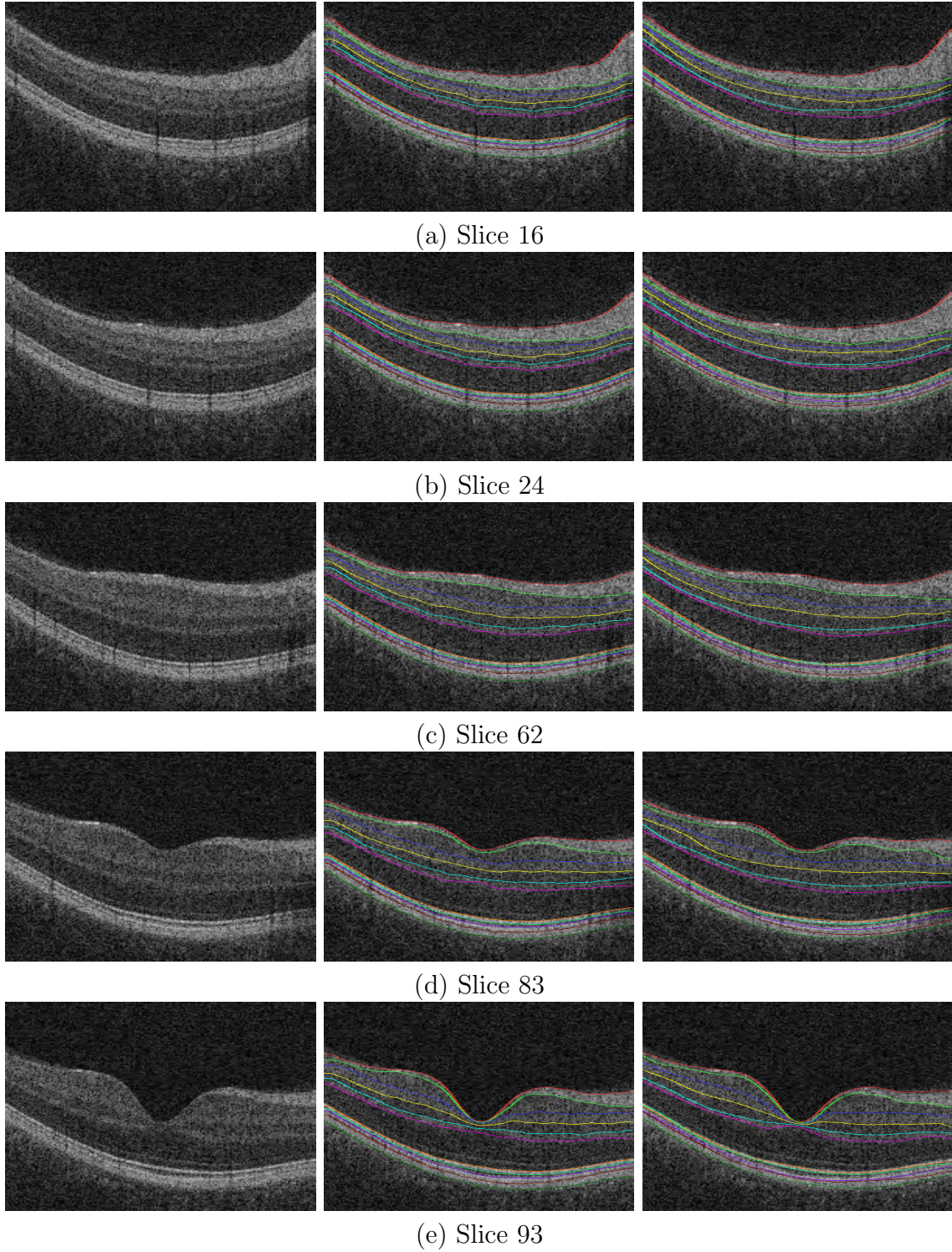
Figure 3.4: Segmentation results of ten intraretinal layers in the best performance case. The first column shows X-Z images of the original OCT volume, and the second and third columns represent our segmentation results and the reference standards, respectively.

(a) Slice 4

(b) Slice 22

(c) Slice 45

(d) Slice 83

(e) Slice 102
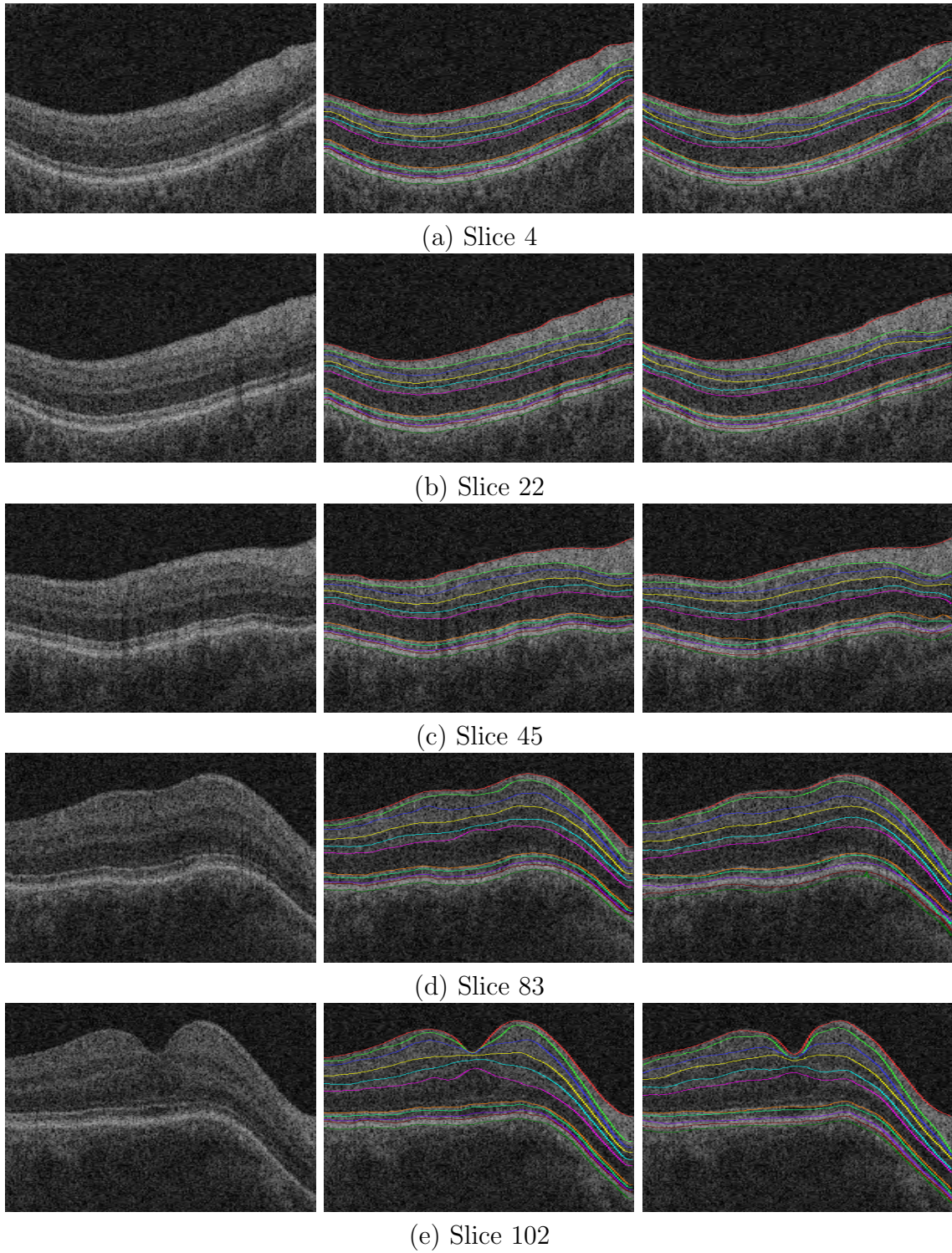
Figure 3.5: Segmentation results of ten intraretinal layers in the worst performance case. The first column shows X-Z images of the original OCT volume, and the second and third columns represent our segmentation results and the reference standards, respectively.

Table 3.5: Mean absolute thicknesses differences between our segmentation results and reference standards, and between manual tracings from two observers (Mean ± SD), and p-values for paired t-tests between these absolute thicknesses differences.

Layer	Algo. vs. Ref. (μm)	Obs. 1 vs. Obs. 2 (μm)	p-value
1-2	7.46 ± 8.76	14.15 ± 15.32	< 0.01
2-3	12.04 ± 10.21	26.10 ± 17.09	< 0.01
3-4	13.92 ± 10.61	34.58 ± 15.52	< 0.01
4-5	7.02 ± 5.34	8.92 ± 7.76	< 0.01
5-6	4.89 ± 4.12	6.98 ± 6.54	< 0.01
6-7	5.79 ± 6.42	8.17 ± 10.56	< 0.01
7-8	3.45 ± 4.48	4.98 ± 9.02	< 0.01
8-9	5.72 ± 4.03	7.20 ± 5.45	< 0.01
9-10	6.41 ± 4.85	8.59 ± 6.31	< 0.01
10-11	7.64 ± 4.32	6.47 ± 4.81	< 0.01
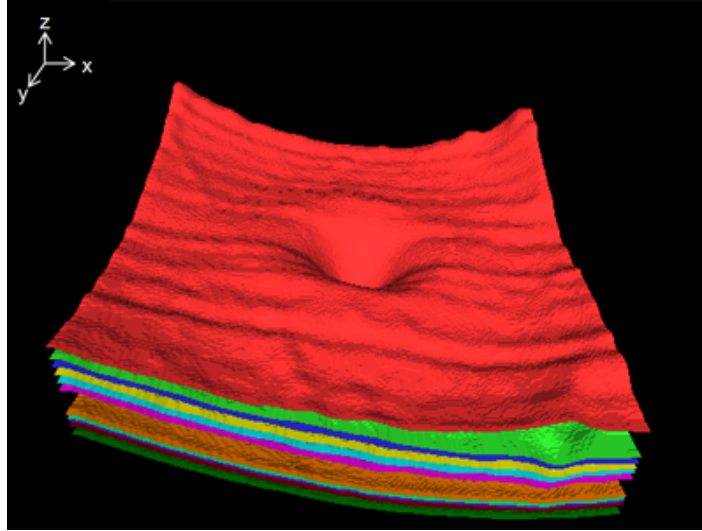
Figure 3.6: 3-D rendering of eleven segmented retinal surfaces in the best performance case.

which have the minimum and maximum sums of unsigned border positioning errors of all retinal surfaces, respectively. In addition, Fig. 3.6 shows the 3-D rendering of eleven segmented retinal surfaces in the best performance case.

3.4   Discussion

We have presented a method to automatically segment eleven retinal surfaces defining ten intraretinal layers in spectral-domain macular OCT scans using a multi-scale 3-D graph search method. The main contribution of this study is development of the fast intraretinal layer segmentation method which deals with several OCT subvolumes instead of a whole OCT volume.

The presented method shows excellent results. From Tables 3.1 and 3.2, the overall mean unsigned mean border positioning error was 2.88 ± 2.55 voxels (5.75 ± 5.11 μm). Surface 3 had a slightly larger mean unsigned bordering positioning error than other surfaces since surfaces 3 are obscured in some cases. However, the mean unsigned bordering positioning error was much smaller than the mean border positioning difference between two manual tracings. Based on Tables 3.3 and 3.4, the small signed border positioning differences in surfaces 1, 5, 6, 10 and 11 are not so meaningful since these surfaces have the significantly larger or similar unsigned border positioning differences compared with the unsigned border positioning errors. In Table 3.5, our method showed a good property of the intraretinal layer thicknesses except layer 10-11.

To the best of our knowledge, Garvin's preliminary method segmented the largest number of intraretinal layers (six layers) of prior approaches with good accuracy in spectral-domain OCT scans [19]. Therefore, the reported method was compared with her method in terms of the number of segmented layers, speed and accuracy. First, our method was capable of detecting four more intraretinal layers than hers. Second, compared with her method requiring over 10 hours (Windows XP Professional x64, Intel Xeon CPU @ 3.2 GHz, 10 GB of RAM), our method required only 70 seconds

(Windows XP Professional x64, Intel Core 2 Duo CPU @ 3.0 GHz, 4 GB of RAM). Finally, our segmentation results showed similar accuracy to her segmentation results in Tables 3.1 and 3.3.

To improve the segmentation accuracy, the addition of regional information to the current edge-based cost function for the 3-D graph search and the multiscale 3-D graph search with varying constraints could be meaningful [19, 20]. The multiscale 3-D graph search method has a limitation in case that some retinal surfaces are invisible in OCT volumes of low resolutions. The method was tested in OCT scans from normal subjects in this study. It needs to be tested in OCT scans from patients having some diseases such as glaucoma, anterior ischemic optic neuropathy (AION) and facioscapulohumeral muscular dystrophy (FSHD) [19].

CHAPTER 4
SEGMENTATION OF THE OPTIC DISC IN 3-D ONH-CENTERED OCT SCANS

4.1 Methods

The method starts by segmenting three retinal surfaces in the original spectral-domain OCT volume using a multiscale 3-D graph search-based method (Fig. 4.1, Section 4.1.1). An OCT projection image was created by averaging in the z-direction the OCT subvolume between surfaces 2 and 3 (Section 4.1.2). The OCT volume, retinal surface segmentation and OCT projection image were used as features for classification of the optic disc cup and neuroretinal rim. The optic disc cup and rim were detected by a contextual k-NN classifier incorporating neighboring A-scans (Section 4.1.3). Finally, prior knowledge about the shapes of the optic disc cup and neuroretinal rim regions was incorporated through the application of convex hull-based fitting (Section 4.1.5).

4.1.1 Segmentation of three retinal surfaces using a multiscale 3-D graph search

Segmentation of three retinal surfaces in ONH-centered OCT volumes is a pre-processing step for our supervised classification-based optic disc cup and rim segmentation method. Surface 1 in Fig. 4.1 represents the depth of the ONH which is a dominant feature of the optic disc cup and rim. Surfaces 2 and 3 are required to create an OCT projection image which is used for creating the optic disc ground truth of the OCT volume (Section 4.1.2). The OCT projection image is also utilized as a feature for optic disc classification of the OCT volume (Section 4.1.3).

We developed a fast multiscale extension of the 3-D graph search method to detect these retinal surfaces in ONH-centered OCT volumes. The basic idea of the multiscale 3-D graph search is to detect the surface in the high resolution using the surface segmented in the low resolution. The method starts by creating five multiscale OCT volumes. The OCT volume in level 5 is the original OCT volume, and that in

<center>(a)   (b)</center>
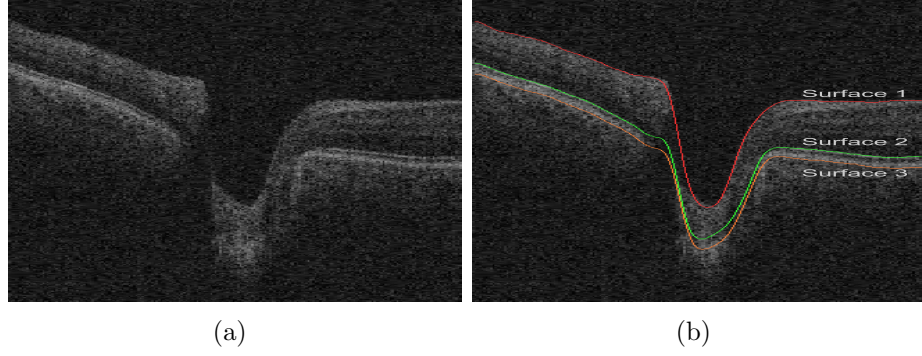
Figure 4.1: Definition of three retinal surfaces (surfaces 1 – 3). (a) X-Z image of the original OCT volume. (b) Image (a) overlapped with three retinal surfaces. Surface 1 is the upper surface of the GCL, surface 2 is the in-between surface of the ICL and CL, and surface 3 is the lower surface of the RPE/BM.

<center>(a)   (b)   (c)</center>

<center>(d)   (e)   (f)</center>
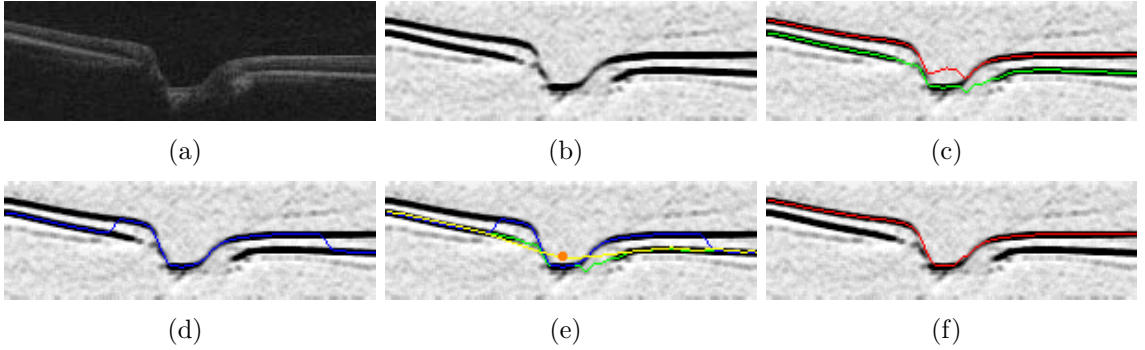
Figure 4.2: Segmentation of surface 1 in level 1. (a) OCT volume in level 1. (b) Cost functions for double and single surface 3-D graph searches. (c) Double surface 3-D graph search result. The top surface (red line) is surface 1, and the bottom surface (green line) is surface 2. (d) Single surface 3-D graph search result. (e) Thin plate spline (yellow line) fitted to surface 2 in image (c) excluding the subsurface close to the center of the optic disc cup and including the control point (orange dot) to guide the thin plate spline. The center of the optic disc cup is the (x, y) location in which the surface (blue line) in image (d) has the lowest z-position, and the control point is, at the center of the optic disc cup, the middle point in the z-axis of the surface in image (d) and the another thin plate spline fitted to surface 2 in image (c) excluding the subsurface close to the center of the optic disc cup. (f) Final surface 1 segmentation result. If the surface in image (d) is lower than the surface located 2 voxels below the thin plate spline (yellow line) in image (e), the z-positions of surface 1 in image (c) were replaced by the surface in image (d).

(a)   (b)

(c)
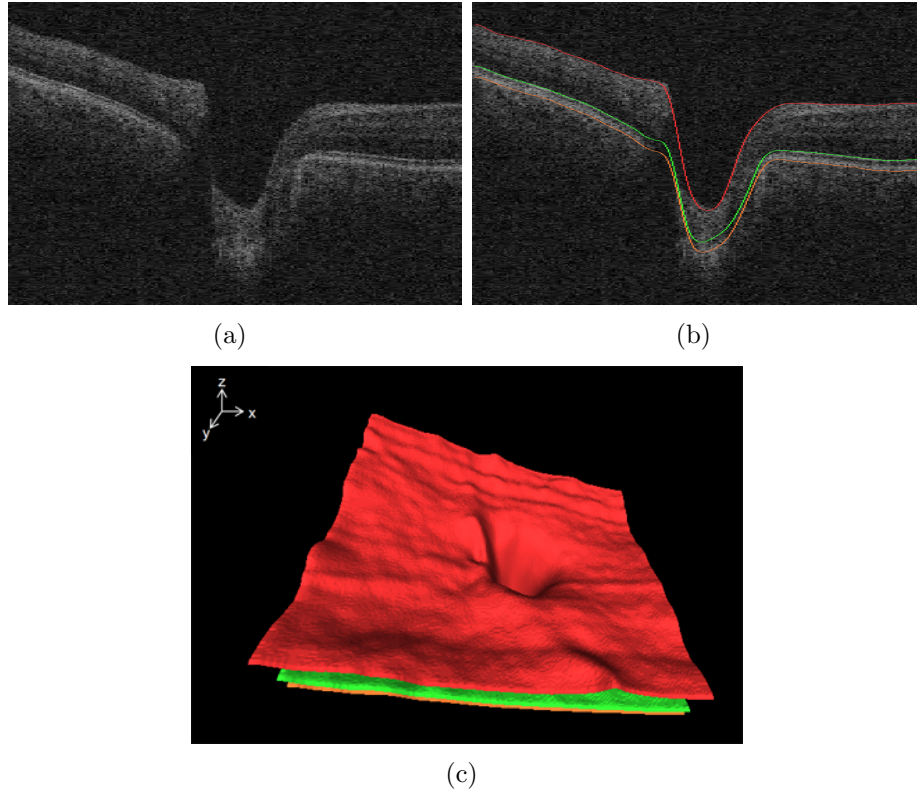
Figure 4.3: Segmentation results of three retinal surfaces in the ONH-centered OCT volume. (a) X-Z image of the original OCT volume. (b) Image (a) overlapped with the segmented retinal surfaces. (c) 3-D rendering of the segmented retinal surfaces.

level 4 was subsampled by a factor of 2 in the z-axis from that in level 5. OCT volumes in levels 3, 2 and 1 were created in the same fashion. Segmentation of surface 1 in level 1 utilized double and single surface 3-D graph search methods (Fig. 4.2). The cost functions for the graph searches were smoothed, inverted gradient magnitudes of the dark-to-bright transition from top to bottom of the OCT volume. To improve the connectivity of surfaces, a $3 \times 3 \times 3$ averaging filter was applied to the gradient magnitude volume, and the smoothed gradient magnitude volume was inverted since the graph search detects optimal surfaces having the minimum cost. The approximate position of surface 1 in level 2 was guided by the z-positions of surface 1 segmented in level 1 multiplied by 2. The accurate position of surface 1 in level 2 was obtained by applying a single surface 3-D graph search to the cost function which was smoothed, inverted gradient magnitudes of the dark-to-bright transition from top to bottom of the OCT subvolume close to the approximate position of surface 1 in level 2. In the same fashion, surfaces 1 in levels 3, 4 and finally 5 were hierarchically detected. Segmentation of surface 2 in level 5 was the same as that of surface 1 except using a double surface 3-D graph search approach based on surface 2 in level 1 (Fig. 4.2(c)). The top surface obtained by the double surface graph search is surface 2, and the bottom surface was used for segmentation of surface 3 in level 5. Surface 3 in level 5 was detected by employing a single surface 3-D graph search to the cost function which was smoothed, inverted gradient magnitudes of the bright-to-dark transition from top to bottom of the OCT subvolume below the bottom surface of the double surface graph search in level 5. Fig. 4.3 shows our segmentation results of three retinal surfaces. In addition, the retinal surface segmentation was performed in the whole OCT volume ($200 \times 200 \times 1024$ voxels) for creating the optic disc reference standard of the ONH-centered OCT scan in Section 4.2.1 and in the partial OCT volume (center $100 \times 100 \times 1024$ voxels) for the optic disc segmentation in Section 4.1.3.

4.1.2   OCT projection image

An OCT projection image is necessary for creating the optic disc ground truth of a spectral-domain OCT scan in Section 4.2.1. In contrast with the unprocessed 3-D OCT scan, the retinal vasculature is visible in the projection image. Feature points derived from the vasculature such as bifurcations can be used to register the fundus image with the OCT volume. Additionally, the projection image provides features for the cup and rim classification of the OCT volume in Section 4.1.3. The OCT projection image was created by averaging in the z-direction the OCT subvolume between surfaces 2 and 3 segmented in Section 4.1.1. These two surfaces define a layer that, due to its position in the retina and high contrast with the retinal background, contains a large number of high contrast vessel shadows [33].

4.1.3   Segmentation of the optic disc using a contextual k-NN classifier

To segment the optic disc cup and neuroretinal rim from the background, a supervised classification method was used. This method assigned one of three labels (i.e. background, cup, rim) to each A-scan in the 3-D OCT scan. A set of ten features, obtained from original OCT volumes and retinal surfaces and OCT projection images were calculated for each A-scan in the OCT volume (Fig. 4.4).

- Features 1 – 6: Average voxel intensities of six local A-scans. One local A-scan consists of 30 voxels in the z-axis. Six local A-scans cover 60 voxels above the thin plate spline fitted to surface 2 excluding the subsurface around the center of the optic disc cup, and 120 voxels below it. The center of the optic disc cup is defined as the (x, y) position of the lowest point of surface 1 in the z-axis.

- Feature 7: Distances between surface 1 and the thin plate spline fitted to surface 2 excluding the subsurface around the center of the optic disc cup, which measure the depth of the ONH.

- Feature 8: OCT projection image, which contains information about the vas-
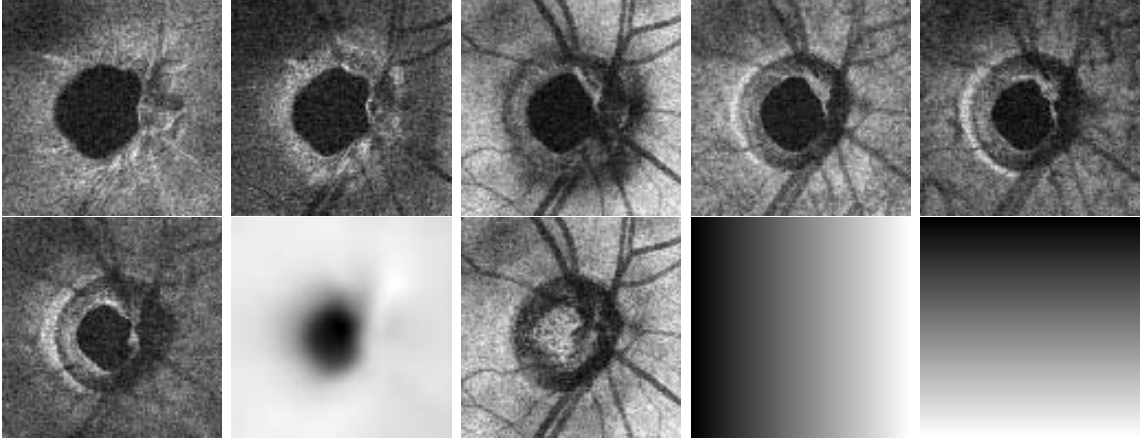
Figure 4.4: Ten features (features 1 – 10 from top left to bottom right). The features were mapped between 0 and 255 for the purpose of visualization. The center 100×100 A-scans of the original ONH-centered OCT volume were used for feature calculation since the ONH is located in this volume.

culature and the location of the neuroretinal rim edge.

- Features 9, 10: Displacements from the center of the optic disc cup in x- and y-directions, which represent the positions of the optic disc cup and rim.

Each feature was normalized to have zero mean and unit variance. A k-NN classifier [3] was used to perform the classification. For each A-scan the classifier determined the k nearest neighbors in the feature space and assigned the most common label amongst the nearest neighbors to the query A-scan (Fig. 4.5(b)).

A-scan classification based on the regular k-NN classifier can result in noisy output due to the fact the classification is based on individual A-scans, and the classifier does not take information from neighboring A-scans into account. From prior knowledge it is known the method should find two 8-connected objects (i.e. the optic disc cup and rim) surrounded by the background. As such one can assume that A-scans that are close together have a high probability of having the same label. This observation led us to incorporate information from neighboring A-scans in the classification of the query A-scan. Instead of just determining the k nearest neighbors for the A-
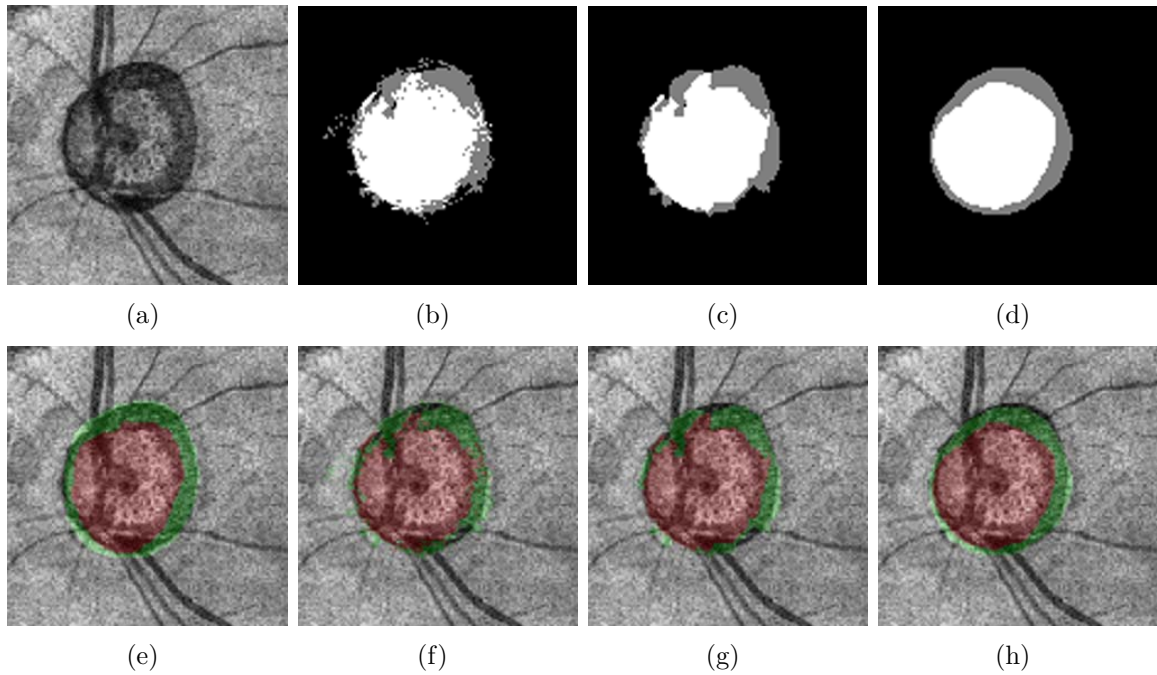
Figure 4.5: Segmentation results of the optic disc cup and neuroretinal rim. (a) OCT projection image. (b) Segmentation result obtained by a 61-NN classifier. The optic disc cup is in white, the neuroretinal rim is in gray, and the background is in black. (c) Segmentation result obtained by a 9-31-NN classifier. (d) Segmentation result obtained by a 9-31-NN classifier with convex hull-based fitting. (e) OCT projection image overlapped with the reference standard. The optic disc cup is in red, and the neuroretinal rim is in green. (f) OCT projection image overlapped with image (b). (g) OCT projection image overlapped with image (c). (h) OCT projection image overlapped with image (d).

scan under consideration, all nearest neighbors for each of the individual A-scans in the 3×3 neighborhood centered on the query A-scan were determined. The most frequent label amongst these nearest neighbors was assigned to the query A-scan (Fig. 4.5(c)). From this point forward, this classification method is referred to as "9-k-NN" classification.

4.1.4 Parameter selection

Parameter selection includes k-value selection for the k-NN, 9-k-NN classifiers and feature selection. Three-fold cross validation was performed using a training set of 44 OCT scans and a testing set of 22 OCT scans. For each fold, the training set was split into 22 OCT training scans and 22 OCT testing scans utilized for the parameter selection. Eleven k-values ($k = 1, 11, \cdots, 101$) were compared in terms of the sum of Dice similarity coefficients (DSCs) of the cup and rim between classification results and reference standards [48]. The DSC measures the spatial overlap between two regions, A and B, and is defined as $DSC(A, B) = 2(A \cap B)/(A + B)$, where $\cap$ is the intersection. In Fig. 4.6, the 61-NN and 9-31-NN classifiers had the maximum sums of DSCs of the cup and rim. The 9-k-NN classification had larger sums of DSCs of the cup and rim than the k-NN classification in the eleven tested k-values. After k-value selection, the feature selection was performed using the sequential forward feature selection algorithm [2]. Table 4.1 shows the features selected for the 9-k-NN classification in three phases. All features were selected since features 2, 3, 4, 7, 9, 10 were useful in all phases, and features 1, 5, 6, 8 were helpful in some phases. In addition, feature 7 representing the depth of the ONH was the most dominant feature in all phases.

4.1.5 Post-processing using convex hulls

To preserve the shapes of the optic disc cup and neuroretinal rim which are known to be semi-circular structures, a local fitting method using the convex hulls of the
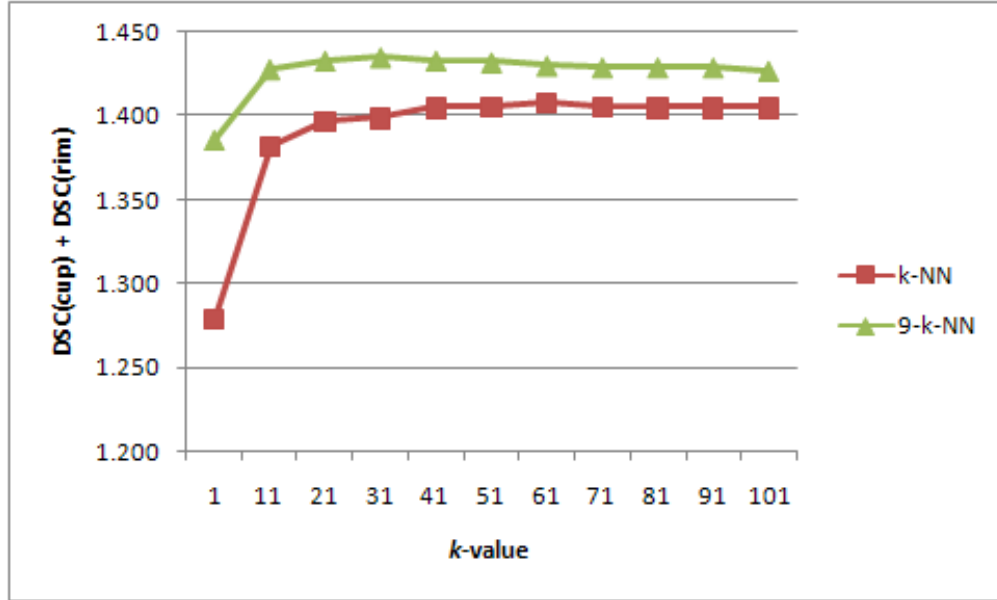
Figure 4.6: The sum of DSCs of the cup and rim according to k-values.

Table 4.1: Selected features for the 9-31-NN classification. The first feature is the most dominant.

Phases	Features
1	7, 4, 2, 3, 1, 10, 9, 6
2	7, 4, 2, 3, 1, 9, 5, 10
3	7, 4, 2, 3, 5, 9, 10, 6, 8

segmentations was developed. This post-processing step was performed to smooth the segmentation results for both the optic disc cup and neuroretinal rim, and Fig. 4.7 visually illustrates the procedure. Fig. 4.7(a) shows the segmentation result obtained by the 9-k-NN classifier. The optic disc cup is used as an example here but the same procedure can be applied to the neuroretinal rim segmentation. The procedure starts by determining the convex hull of the segmentation (Fig. 4.7(b)). To detect the innermost boundary of the segmented object, we turn it "inside-out". Each edge point located at distance r from the center (Fig. 4.7(c)) is relocated to a position $R - r$ from the center (Fig. 4.7(d)). Here R is the radius of a circle around the segmentation, and the circle should be large enough so that it covers the segmentation. We define it such that $R = 2 \times \max(r)$. The red line in Fig. 4.7(e) indicates the convex hull of the inside-out segmentation edge. The innermost boundary of the segmentation edge (the red line in Fig. 4.7(f)) was acquired by inversely applying the previously described transformation to the convex hull in Fig. 4.7(e). The line in between the inner and outer borders (the red line in Fig. 4.7(h)) formed the final segmentation result.

4.2   Experiments

4.2.1   Data

66 × 2 spectral-domain ONH-centered OCT scans were acquired from both the eyes of 33 glaucoma patients at the University of Iowa using Cirrus HD-OCT (Carl Zeiss Meditec, Inc., Dublin, CA, USA) machines. Two repeated OCT scans were obtained for each eye. Dataset 1 consisting of the first 66 OCT scans was used for measuring the accuracy of our segmentation results, and dataset 2 consisting of the second 66 OCT scans was used for only measuring cup-to-disc ratio reproducibility. Each spectral-domain OCT scan consists of 200 × 200 × 1024 voxels covering 6 × 6 × 2 mm³, the voxel size is 30 × 30 × 2 μm, and the voxel depth is 8 bits in grayscale. We also acquired 66 stereo color photograph pairs of the optic disc on the same day of
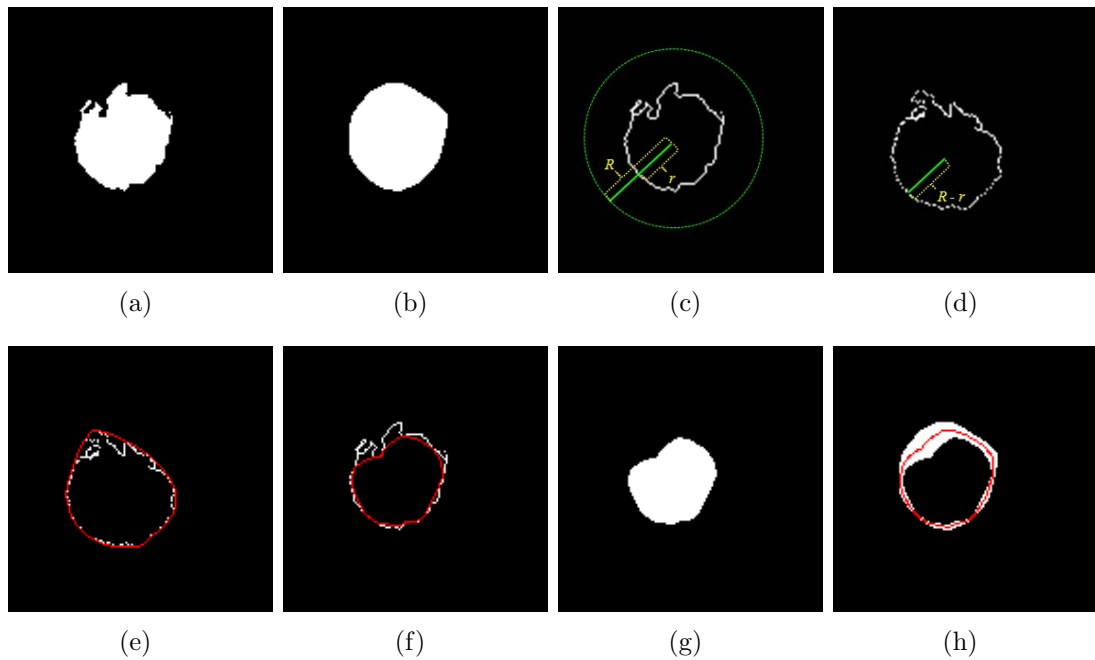
Figure 4.7: Convex hull-based fitting. (a) Optic disc cup segmentation result obtained by a 9-k-NN classifier. (b) Outermost region surrounded by the convex hull of the segmentation in image (a). (c) Edge of the segmentation in image (a). Here, r is the distance between the center of the optic disc cup and the edge of the segmentation in image (a), and R is the radius of the circle whose origin is the center of the optic disc cup. The R is the maximum r multiplied by 2. (d) Edge replaced r with $R - r$ based on the center of the optic disc cup. (e) B-spline (red line) connecting the convex hull of image (d). (f) Innermost boundary (red line). (g) Innermost region. (h) The middle boundary (red line) that forms the final segmentation result.

the same patients, corresponding to the spectral-domain OCT scans, using a stereo-base Nidek 3Dx stereo retinal camera (Nidek, Newark, NJ, USA). The size of the stereo color photographs is 4096 × 4096 pixels, and the pixel depth is 3 × 8-bit red, green and blue channels. The Institutional Review Board of the University of Iowa approved the research protocol.

Since it is difficult for glaucoma specialists to directly delineate the optic disc cup and neuroretinal rim margins in spectral-domain OCT scans, they were indirectly acquired from an optic disc reference standard of stereo color photographs. The optic disc reference standard of the stereo color photographs was created by optic disc manual tracings obtained from three glaucoma experts in a "majority-win" manner to reduce substantial inter-observer variability (Fig. 4.8) [26]. In other words, the optic disc reference standard of the stereo color photographs was created by selecting the most common cup and rim labels of three optic disc manual tracings for each pixel.

Fig. 4.9 shows how to create the optic disc reference standard of the spectral-domain OCT scan from that of the stereo color photographs. One of a pair of stereo color photographs (Fig. 4.9(a)) was registered onto the corresponding OCT projection image (Fig. 4.9(c)) by manually indicating two correspondence points in both the stereo color photograph and OCT projection image (Fig. 4.9(d)). After registration, the optic disc reference standard of the spectral-domain OCT scan (Fig. 4.9(e)) was obtained by applying the same transformation to that of the stereo color photographs (Fig. 4.9(b)).

4.2.2 Validation

To evaluate our optic disc cup and neuroretinal rim segmentation approach, three-fold cross validation was performed on datasets 1 and 2 consisting of 66 × 2 spectral-domain OCT scans using a training set from dataset 1 (see Section 4.1.4). Our optic disc segmentation result was compared with the reference standard of the spectral-
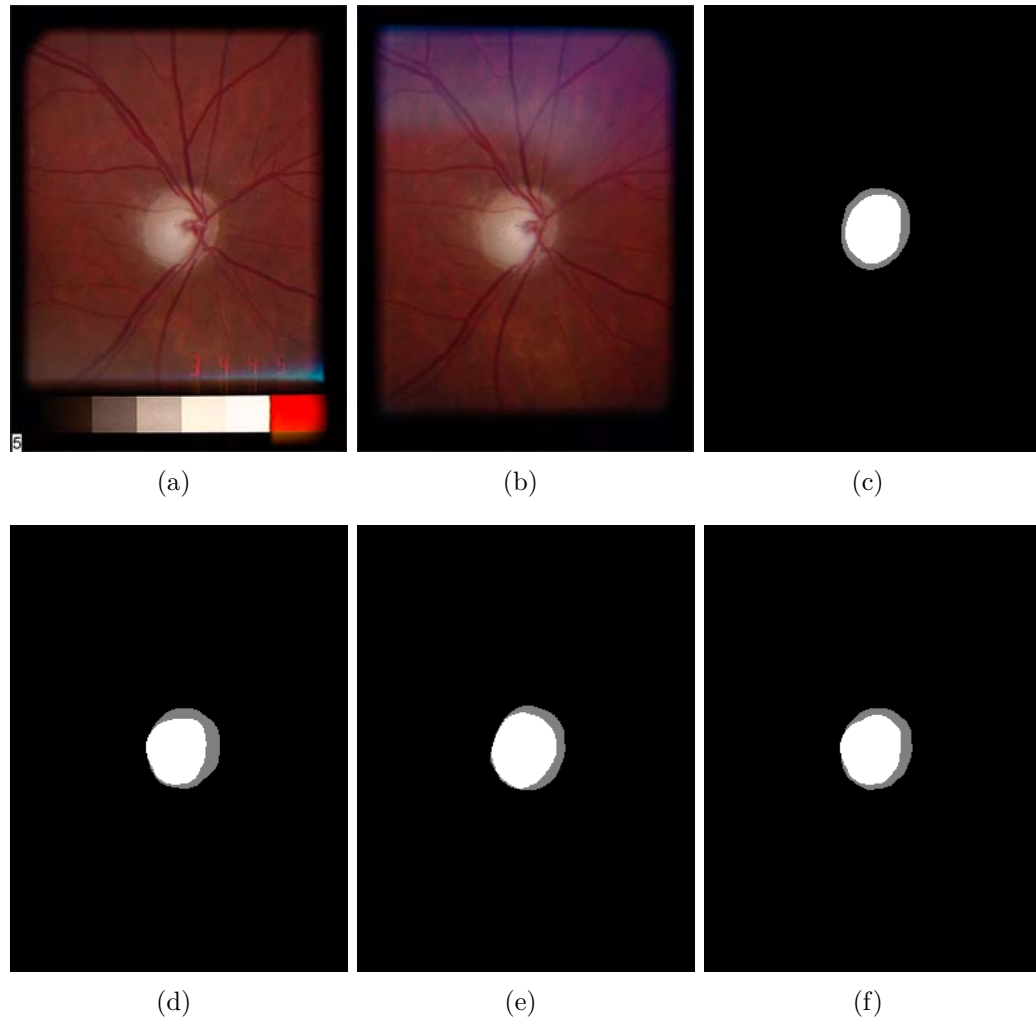
Figure 4.8: Reference standard obtained from optic disc manual tracings of stereo color photographs delineated by three glaucoma experts. (a) One of a pair of stereo color photographs. (b) The other of a pair of stereo color photographs. (c) Manual tracing 1. The optic disc cup is in white, and the neuroretinal rim is in gray. (d) Manual tracing 2. (e) Manual tracing 3. (f) Reference standard.

(a)   (b)   (c)

(d)   (e)
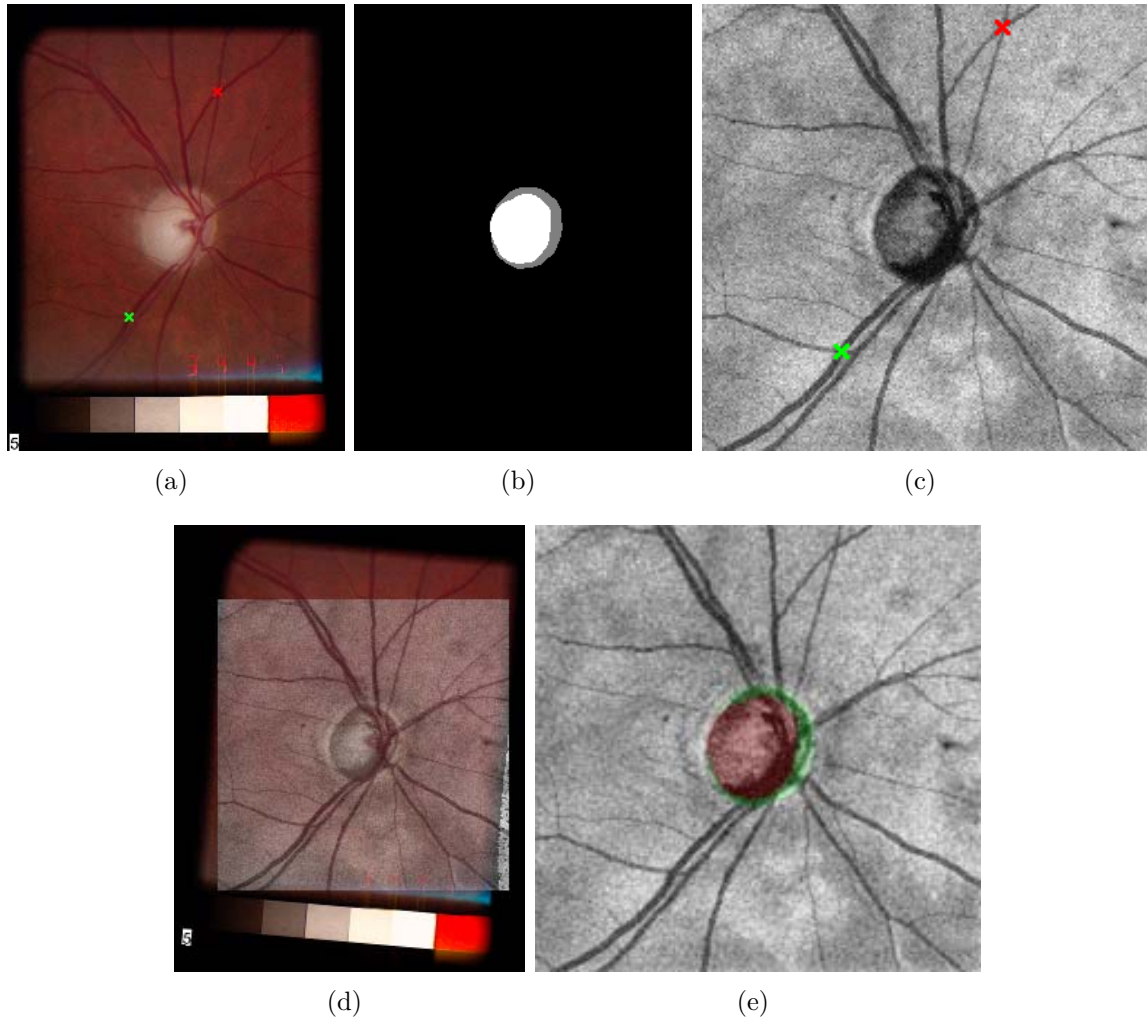
Figure 4.9: Optic disc reference standard of the spectral-domain OCT scan. (a) One of a pair of stereo color photographs from Fig. 4.8(a). The red and green markers are correspondence points for registration. (b) Optic disc reference standard of image (a) from Fig. 4.8(f). The optic disc cup is in white, and the neuroretinal rim is in gray. (c) OCT projection image. (d) Image (a) registered onto image (c). (e) OCT projection image overlapped with the optic disc reference standard of the OCT scan. The optic disc cup is in red, and the neuroretinal rim is in green.

domain OCT scan. The accuracy of our optic disc segmentation result was estimated by measuring DSC, unsigned/signed border positioning errors and cup-to-disc ratio (CDR). The unsigned border positioning errors of the optic disc cup and neuroretinal rim were calculated by measuring the closest Euclidean distances between all edge points from our segmentation result and those from the reference standard. The signed border positioning errors of the optic disc cup and neuroretinal rim were calculated by the differences in the Euclidean distance to the center of the optic disc cup. If the distance of an edge point from our segmentation result to the center of the optic disc cup is shorter than that of an edge point from the reference standard to the center of the optic disc cup, the signed border positioning error is negative, otherwise positive. Note that these unsigned/signed border positioning errors can only be calculated after convex hull-based fitting has been applied. The CDR was defined as $\sqrt{n_c/(n_r + n_c)}$, where n_c is the number of pixels in the cup, and n_r is the number of pixels in the rim [1].

To validate our optic disc segmentation method, the DSC, unsigned/signed border positioning errors and CDR of our segmentation result were compared with the DSC, unsigned/signed border positioning differences and CDR among three manual tracings registered in the same manner as the reference standard of the spectral-domain OCT scan. After confirming the normal distributions of two datasets by the Shapiro-Wilk test, a paired t-test was used in the 95% confidence interval to compare these two datasets.

Finally, CDR reproducibility was evaluated by the absolute CDR differences of the repeated OCT scans from datasets 1 and 2.

4.3   Results

From Table 4.2, in comparison between k-NN and 9-k-NN classifiers, the 9-k-NN classifier showed significantly larger DSCs for both the optic disc cup ($p < 0.01$) and neuroretinal rim ($p < 0.01$). The DSCs from the 9-k-NN classifier with convex hull-

Table 4.2: Mean Dice similarity coefficients (DSCs) (Mean ± SD).

	61-NN vs. Ref.	9-31-NN vs. Ref.	9-31-NN + Convex vs. Ref.
Cup	0.784 ± 0.213	0.792 ± 0.221	0.827 ± 0.166
Rim	0.625 ± 0.142	0.643 ± 0.153	0.675 ± 0.151
	Obs. 1 vs. 2	Obs. 1 vs. 3	Obs. 2 vs. 3
Cup	0.791 ± 0.174	0.806 ± 0.123	0.817 ± 0.154
Rim	0.580 ± 0.171	0.508 ± 0.216	0.644 ± 0.181

Table 4.3: Mean unsigned border positioning errors between our segmentation results and reference standards, and mean unsigned border positioning differences between two manual tracings from three observers (Mean ± SD).

	Algo. vs. Ref.	Obs. 1 vs. 2	Obs. 1 vs. 3	Obs. 2 vs. 3
Cup (pixel)	2.46 ± 1.01	3.02 ± 1.38	3.33 ± 1.29	3.05 ± 1.66
Cup (mm)	0.07 ± 0.03	0.09 ± 0.04	0.10 ± 0.04	0.09 ± 0.05
Rim (pixel)	2.06 ± 0.97	3.59 ± 1.30	3.01 ± 1.31	1.96 ± 0.92
Rim (mm)	0.06 ± 0.03	0.11 ± 0.04	0.09 ± 0.04	0.06 ± 0.03

based fitting were significantly larger than those from the 9-k-NN classifier for the cup ($p < 0.01$) and rim ($p < 0.01$). While the DSCs from the 9-k-NN classifier with convex hull-based fitting were not significantly different from those between observers 2 and 3 for the cup ($p > 0.41$), they were significantly larger for the rim ($p < 0.04$).

Based on Table 4.3, optic disc cup segmentation results from our method using a 9-k-NN classifier with convex hull-based fitting have significantly smaller unsigned border positioning errors than any combination of three observers ($p < 0.01$). In neuroretinal rim segmentation results, the unsigned border positioning errors from our method were significantly smaller than the unsigned border positioning differences of observers 1 vs. 2 ($p < 0.01$) and observers 1 vs. 3 ($p < 0.01$) but they were not significantly different from the unsigned border positioning differences of observers 2 vs. 3 ($p > 0.65$).

From Table 4.4, for the optic disc cup, the signed border positioning errors from

Table 4.4: Mean signed border positioning errors between our segmentation results and reference standards, and mean signed border positioning differences between two manual tracings from three observers (Mean $\pm$ SD).

	Algo. vs. Ref.	Obs. 1 vs. 2	Obs. 1 vs. 3	Obs. 2 vs. 3
Cup (pixel)	0.52 ± 1.61	0.09 ± 1.92	2.30 ± 1.64	2.47 ± 2.23
Cup (mm)	0.02 ± 0.05	0.00 ± 0.06	0.07 ± 0.05	0.07 ± 0.07
Rim (pixel)	0.17 ± 1.32	2.65 ± 1.33	1.28 ± 1.01	-1.32 ± 1.34
Rim (mm)	0.01 ± 0.04	0.08 ± 0.04	0.04 ± 0.03	-0.04 ± 0.04

Table 4.5: Mean cup-to-disc ratios (Mean $\pm$ SD).

	CDR
Algo.	0.694 ± 0.171
Ref.	0.694 ± 0.159
Obs. 1	0.714 ± 0.128
Obs. 2	0.633 ± 0.175
Obs. 3	0.756 ± 0.166

our method were significantly larger than the signed positioning differences of observers 1 vs. 2 ($p < 0.01$) and smaller than the signed positioning differences of observers 1 vs. 3 ($p < 0.01$) and observers 2 vs. 3 ($p < 0.01$). For the neuroretinal rim, the signed border positioning errors from our method were significantly smaller than the signed positioning differences from any combination of three observers ($p < 0.01$).

Based on Table 4.5, there were not significant CDR differences between our segmentation results and the reference standards. However, there were significant CDR differences among manual tracings from three observers ($p < 0.01$). Fig. 4.10 shows four scatter-plots of CDRs between our segmentation results and the reference standards, and between two manual tracings from three observers. The slope of the trendline of CDRs between our segmentation results and the reference standards is much closer to 1 than those of the trendlines of CDRs between two manual tracings from three observers.
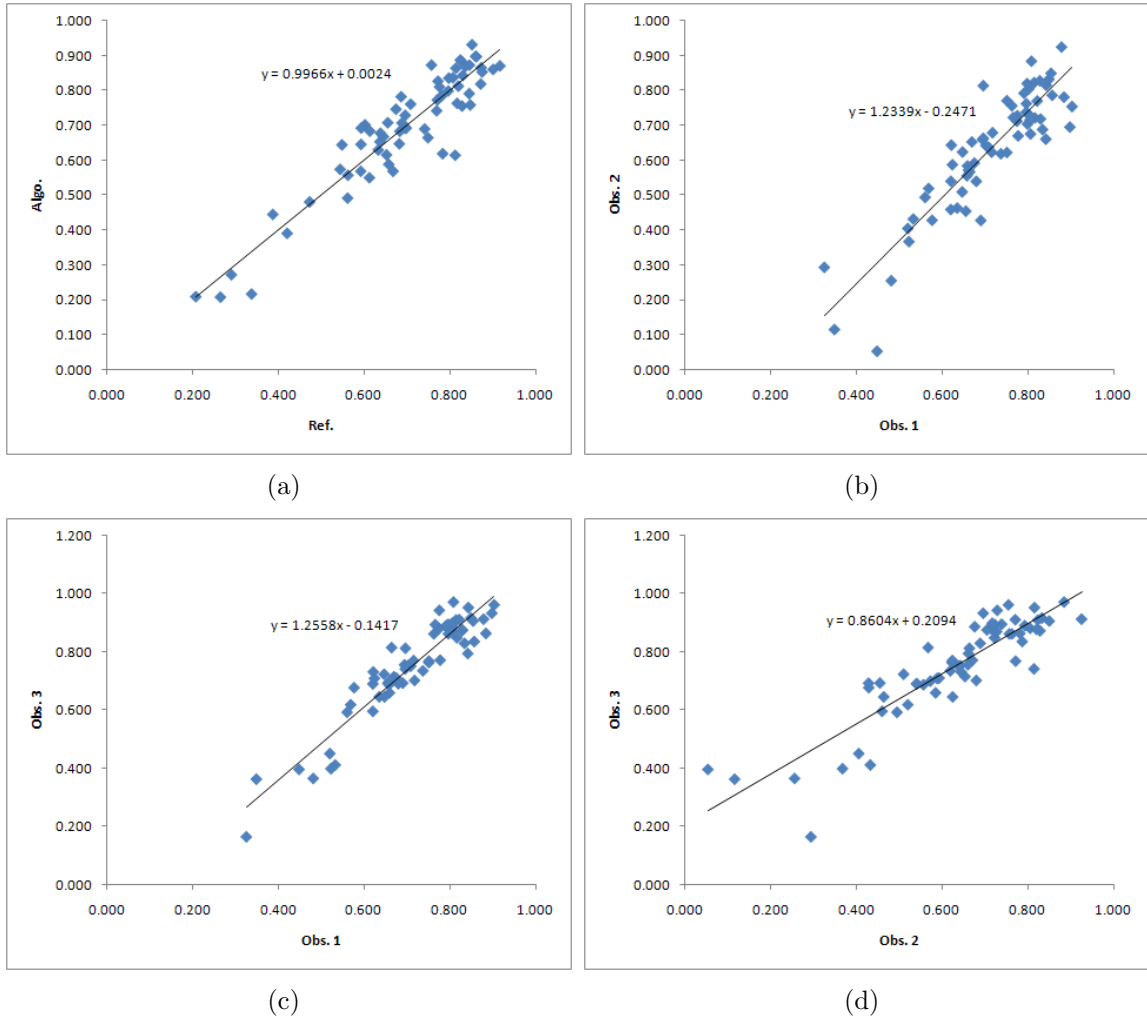
Figure 4.10: Scatter-plots of CDRs. (a) Between the reference standard and algorithm. (b) Between observers 1 and 2. (c) Between observers 1 and 3. (d) Between observers 2 and 3.
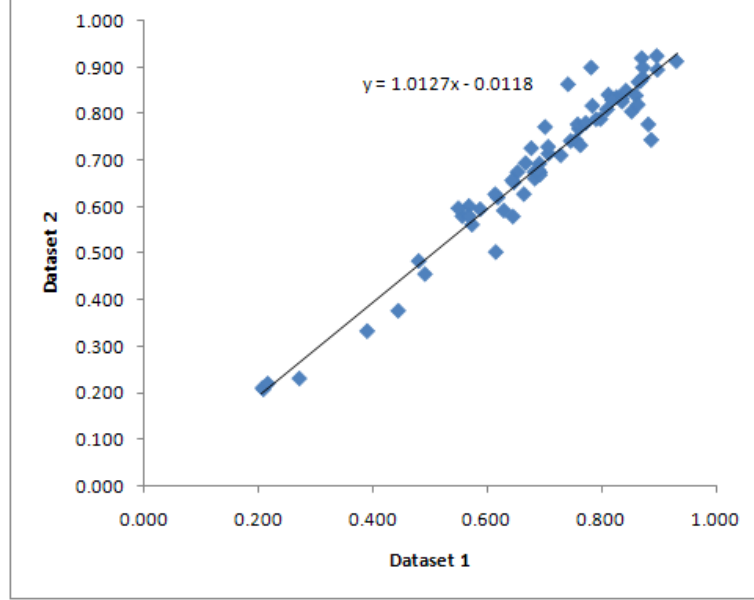
Figure 4.11: Scatter-plot of CDRs between datasets 1 and 2.

The CDR reproducibility of our method between datasets 1 and 2 is $2.8 \pm 3.2\%$. Fig. 4.11 shows the scatter-plot of CDRs between datasets 1 and 2, and the slope of the trendline of CDRs between datasets 1 and 2 is close to 1.

Figs. 4.12 and 4.13 show our optic disc segmentation results of the best and worst performance which have the minimum and maximum sums of unsigned border positioning errors of the optic disc cup and neuroretinal rim, respectively.

4.4   Discussion

We have presented a method to automatically segment the optic disc cup and neuroretinal rim surfaces in ONH-centered 3-D spectral-domain OCT volumes. The method uses a multiscale 3-D graph search method to segment the retinal surfaces and a k-NN classifier that employs contextual information combined with convex hull-based fitting to segment the optic disc cup and neuroretinal rim.

The necessity of the contextual k-NN classifier and convex hull-based post-processing was confirmed in terms of DSCs (Table 4.2). The presented results show that the

(a)   (b)   (c)
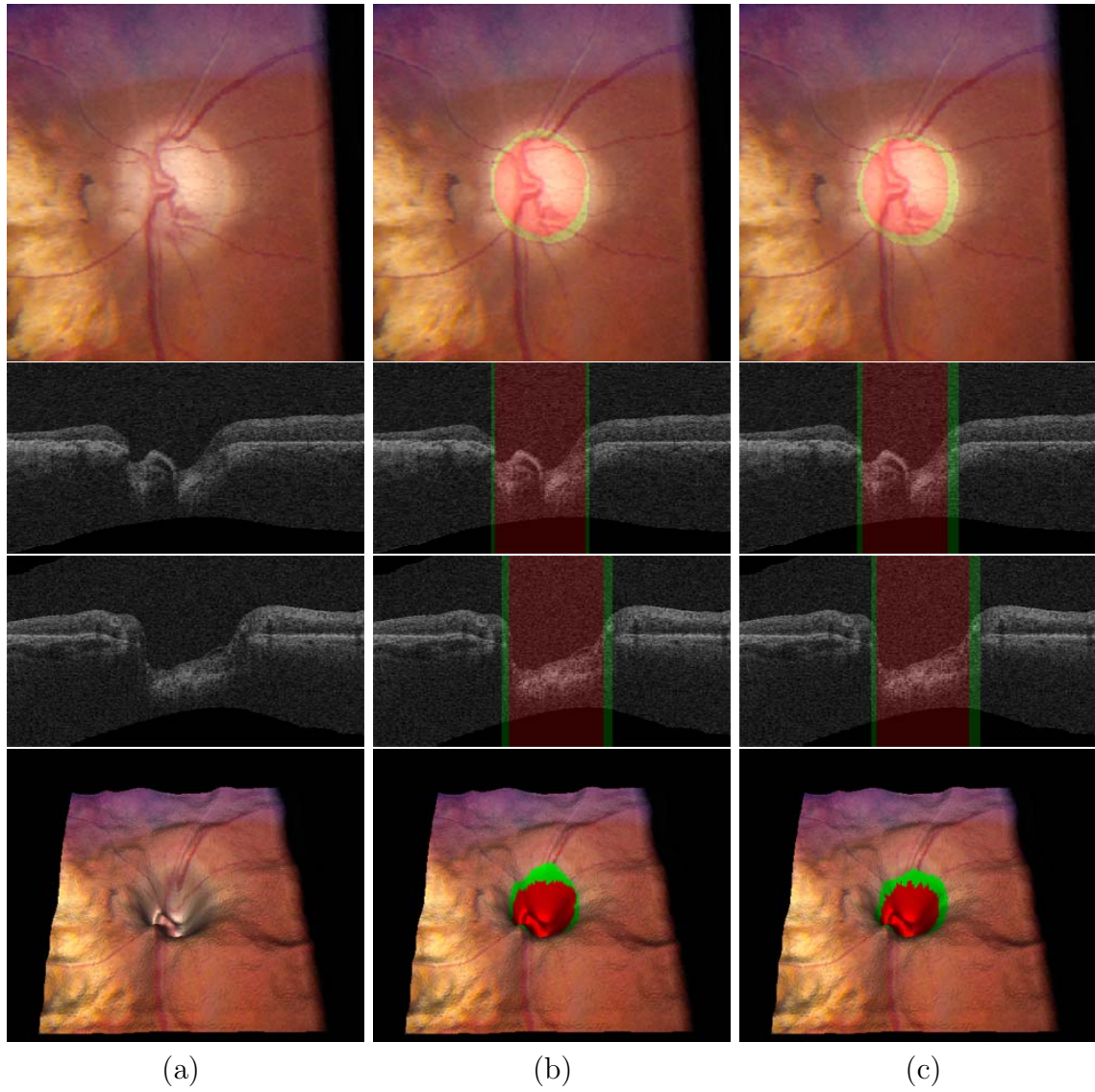
Figure 4.12: Segmentation results of the optic disc in the best performance case (unsigned border positioning error for the optic disc cup = 0.73 pixels (0.022 mm) and unsigned border positioning error for the neuroretinal rim = 1.13 pixels (0.034 mm)). From top to bottom, stereo color photograph, X-Z and Y-Z images at the center of the OCT volume and 3-D rendering of the top retinal surface (surface 1) mapped with the stereo color photograph. (a) Without any overlap. (b) Overlapped with our segmentation result. The optic disc cup is in red, and the neuroretinal rim is in green. (c) Overlapped with the reference standard.
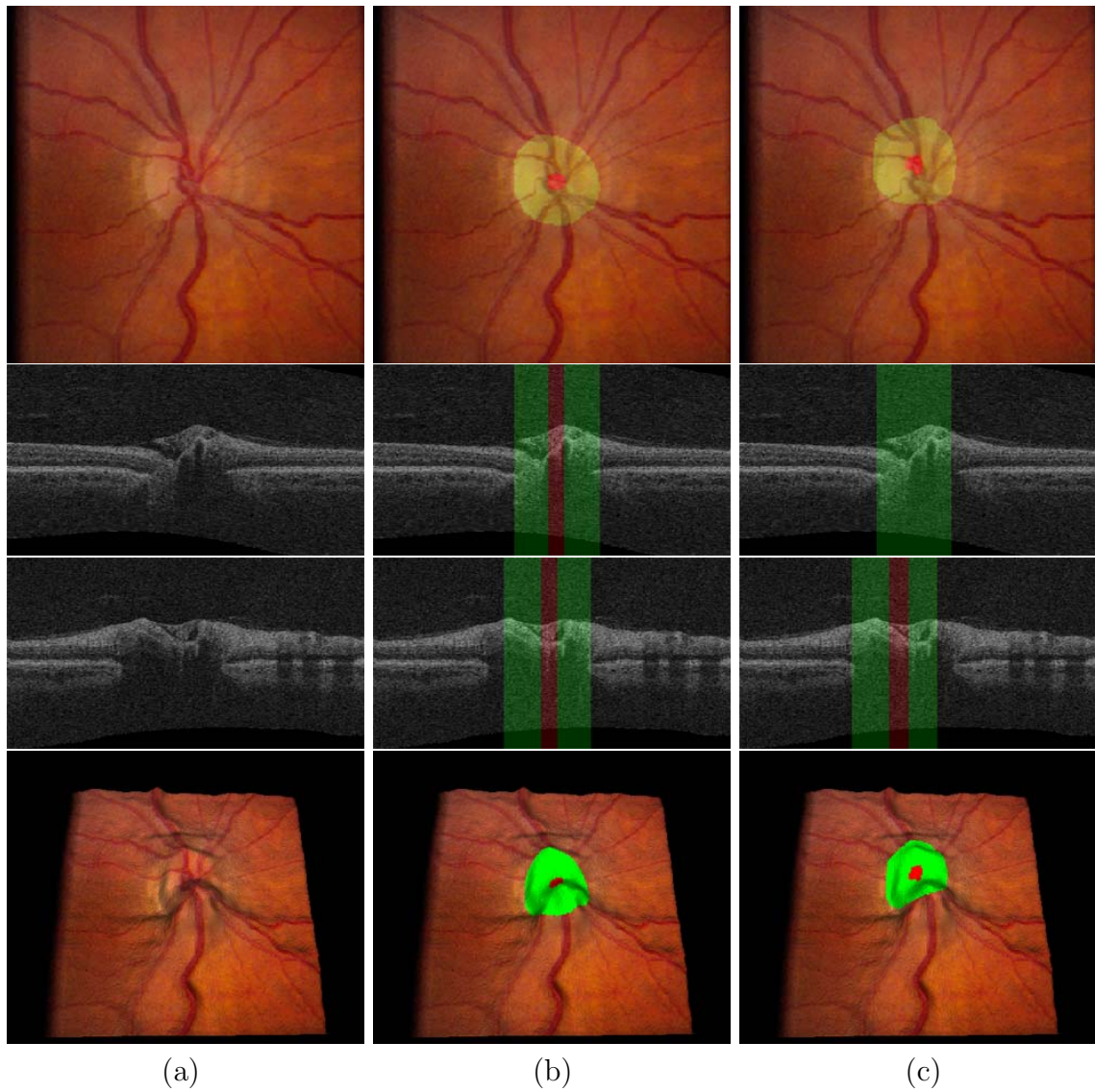
Figure 4.13: Segmentation results of the optic disc in the worst performance case (unsigned border positioning error for the optic disc cup = 5.44 pixels (0.163 mm) and unsigned border positioning error for the neuroretinal rim = 6.38 pixels (0.191 mm)). From top to bottom, stereo color photograph, X-Z and Y-Z images at the center of the OCT volume and 3-D rendering of the top retinal surface (surface 1) mapped with the stereo color photograph. (a) Without any overlap. (b) Overlapped with our segmentation result. The optic disc cup is in red, and the neuroretinal rim is in green. (c) Overlapped with the reference standard.

contextual k-NN classifier outperforms the regular k-NN classifier ($p < 0.01$ for both the cup and rim) when no post-processing is applied. If post-processing is applied, the contextual classifier has significantly larger DSCs on both the cup ($p < 0.01$) and rim ($p < 0.01$) segmentations. In addition, the use of post-processing also improves the pixelated appearance of the segmentation result.

The method shows excellent results when compared with the inter-observer variability among three observers in terms of DSCs, unsigned/signed border positioning errors and CDRs (Table 4.2, 4.3, 4.4, 4.5 and Fig. 4.10). The DSCs, unsigned/signed errors and CDRs between our segmentation results and the reference standards are similar or significantly better than those between two manual tracings from three observers except the signed border positioning errors for the cup. However, the small signed border positioning differences for the cup between observers 1 and 2 in Table 4.4 is not meaningful in this case since the unsigned border positioning differences for the cup in Table 4.3 is large. In other words, manual cup tracings from observers 1 and 2 have a large variation with a small bias. In addition, the method has a good CDR reproducibility between the repeated scans from datasets 1 and 2 ($2.8 \pm 3.2\%$, Fig. 4.11).

In general the method shows good performance. Some issues remain with the ability of the method to adapt to normal anatomical variations inside the ONH. The shape of the ONH in 3-D is similar across the patients in this study. However, the width and depth of the optic cup do vary considerably. The ONH in the best performing case (see Fig. 4.12) has a very wide optic disc cup, and a vessel is running along the cup disturbing the ONH depth measurement. This example illustrates one of the largest issues for the current method. Vessels near the ONH tend to be wide, and they can run partially along the optic disc cup disturbing the local geometry and depth measurements. This in turn can lead to misclassified A-scans on the vessels and a less accurate cup or rim border location. The problem would be alleviated by

including the output of a vessel segmentation system applied to the OCT projection image in the feature set. Another largest issue for the current method is how to deal with non-typical OCT scans having a small optic cup (see Fig. 4.13). The dominant features of typical OCT scans such as the depth of the ONH are useless in the non-typical OCT scans. Therefore, more study on the features which are useful for the non-typical OCT scans is required. In this study, 8 non-typical scans having a small optic cup like Fig. 4.13 out of the 132 OCT scans were included in the experimental data.

There are a number of other possible improvements to the system. The retinal surface segmentation results are a possible source of errors. When large variations in the surface are present, segmentation errors can occur, and this can influence the depth measurements within the ONH. This is primarily an issue for the top retinal surface (surface 1). Another possible source of errors comes from the optic disc reference standard of the OCT scan. When an color stereo photograph was registered onto the OCT projection image, a similarity transformation using two correspondence point pairs of the stereo color photograph and OCT projection image was used. Higher-order transformations such as a quadratic model might improve the registration accuracy [7]. Several additions to the basic graph search algorithm as used in this work can be considered. The addition of regional information to the edge-based cost function for the 3-D graph search could potentially increase the segmentation accuracy [19, 20].

The average processing time of the complete method is 20 seconds. The segmentation of three retinal surfaces using a multiscale 3-D graph search approach takes approximately 15 seconds, and the feature extraction, classification and post-processing requires total 5 seconds. The method was implemented using C++ (Windows XP Professional x64, Intel Core 2 Duo CPU @ 3.00 GHz, 4 GB of RAM). As the implementation was not optimized for speed, additional speed improvements can be

expected.

To summarize, we have presented a method for the segmentation of the optic disc cup and neuroretinal rim from 3-D spectral OCT scans centered at the ONH. The accuracy of the method is similar or significantly better than the inter-observer variability.

CHAPTER 5
SEGMENTATION OF THE RETINAL BLOOD VESSELS IN 3-D ONH-CENTERED OCT SCANS

5.1   Methods

We developed an automated method that can segment 3-D retinal blood vessels from ONH-centered OCT scans using a triangular mesh-based 3-D graph search method. The method starts by detecting three retinal surfaces using a multiscale 3-D graph search method (Fig. 5.1, Section 5.1.1). To have a consistent retinal shape across scans and patients, and reduce eye movement artifacts, the original OCT volume and segmented retinal surfaces are flattened using surface 2 (Section 5.1.2). An OCT projection image including high-contrast vessel shadows is created by averaging in the z-direction the OCT subvolume between surfaces 2 and 3 (Section 5.1.4). A vessel probability map is obtained by applying the supervised pixel classification-based vessel segmentation method to the OCT projection image [33]. The thresholded vessel probability map in which small regions are deleted gives the 2-D positions of the retinal blood vessels. The triangular mesh of an initial 3-D vessel model is built using the thresholded vessel probability map and surfaces 1 and 2. A 3-D graph is constructed in which columns are resampled along the average normal directions of surrounding triangles in the triangular mesh (Section 5.1.5). Finally, the 3-D retinal blood vessels are detected by applying a triangular mesh-based 3-D graph search to the cost function composed of gradient magnitudes of the isotropic OCT scan and OCT projection image.

5.1.1   Segmentation of three retinal surfaces

This section is the same as Section 4.1.1 in Chapter 4.

5.1.2   Flattening of the retinal OCT volume

Spectral-domain ONH-centered OCT volumes have various retinal shapes depending on the eyeball shape, scan position and eye movements. Flattening of the OCT

(a)

(b)

(c)
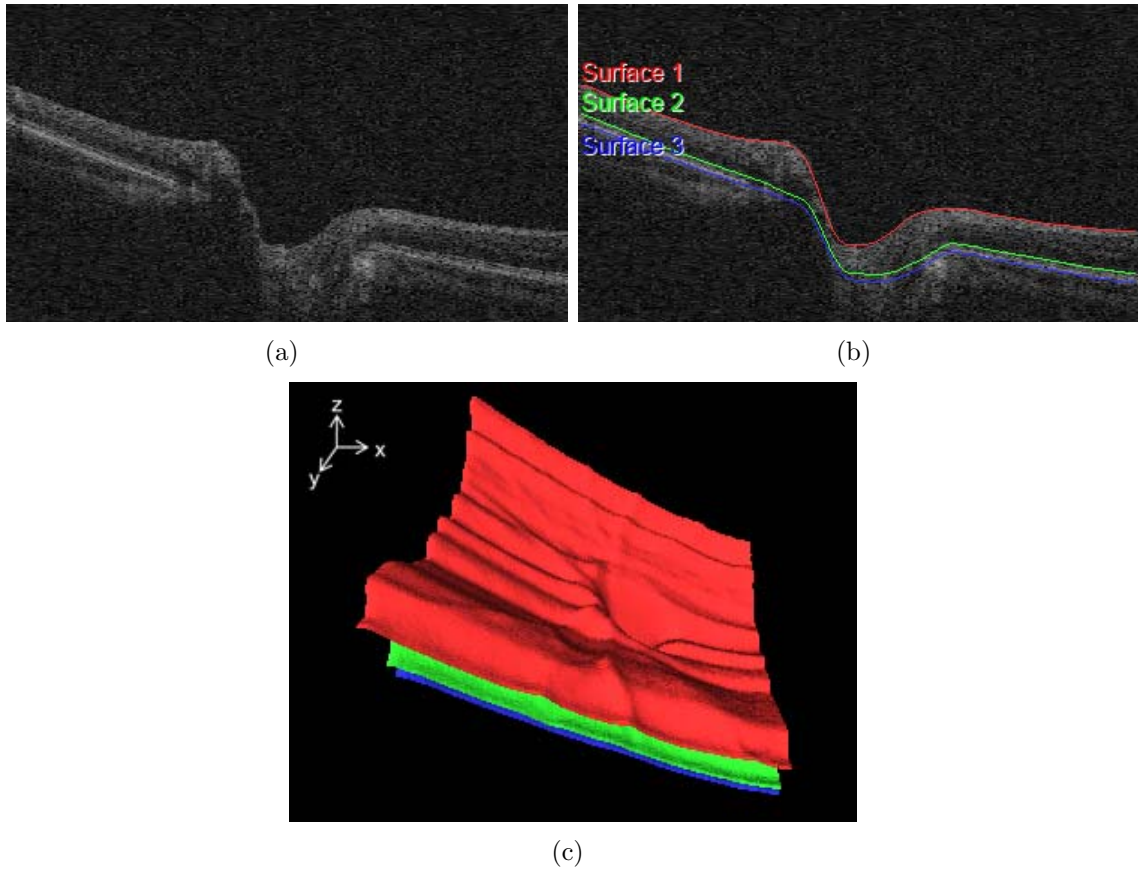
Figure 5.1: Segmentation of three retinal surfaces in the spectral-domain ONH-centered OCT volume. (a) X-Z image of the original OCT volume. (b) Image (a) overlapped with the segmented retinal surfaces. (c) 3-D rendering of the segmented retinal surfaces. Surface 1 is the upper surface of the GCL, surface 2 is the in-between surface of the ICL and CL, and surface 3 is the lower surface of the RPE/BM.

(a)

(b)

(c)

(d)
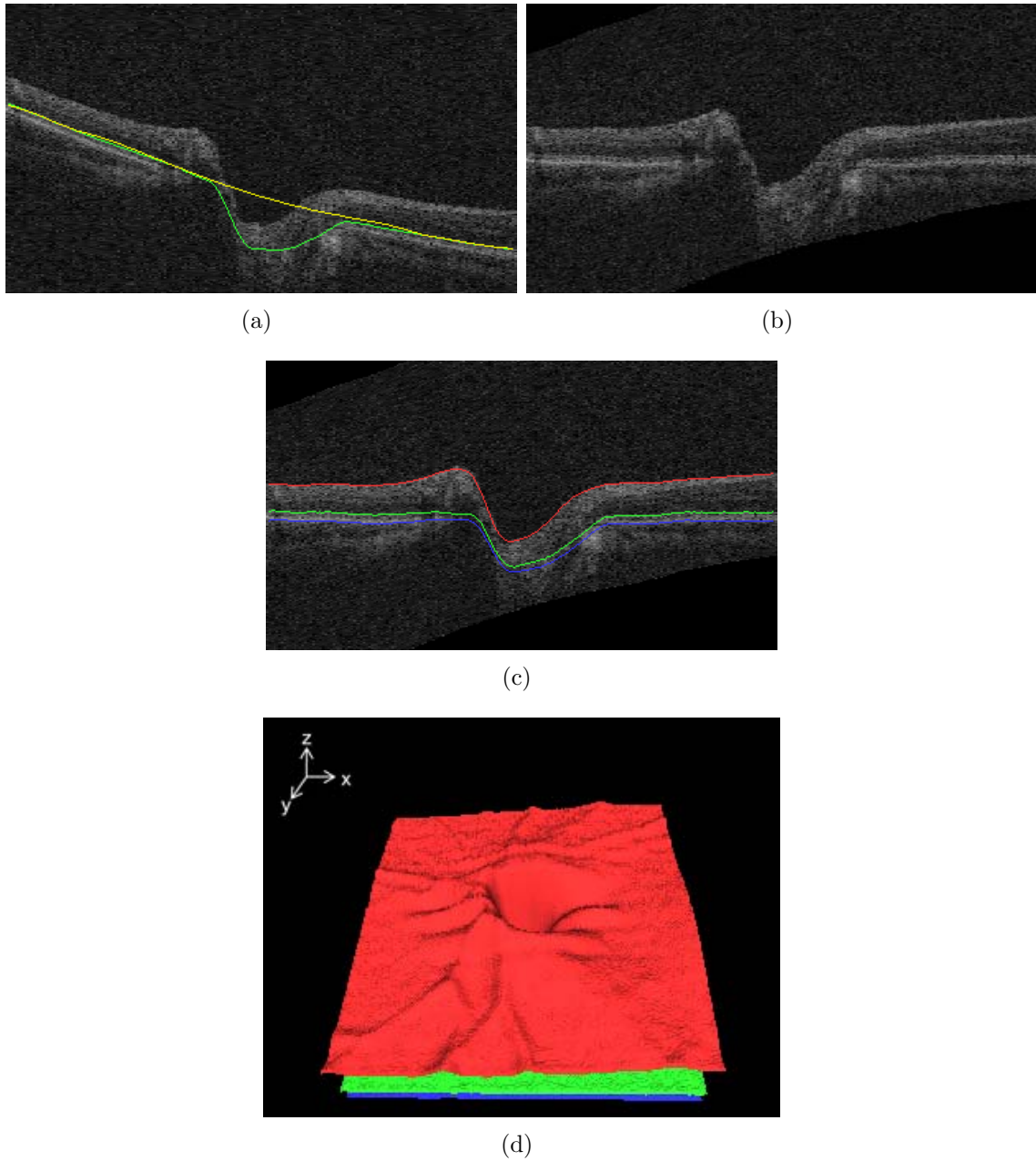
Figure 5.2: Flattening of the retinal OCT volume. (a) Thin plate spline (yellow line) fitted to surface 2 (green line) excluding the subsurface close to the center of the optic disc cup. (b) X-Z image of the flattened OCT volume. (c) X-Z image of the flattened OCT volume overlapped with the transformed retinal surfaces. (d) 3-D rendering of the transformed retinal surfaces. Compared with Fig. 5.1(c), eye movement artifacts existing in the y-axis were reduced.
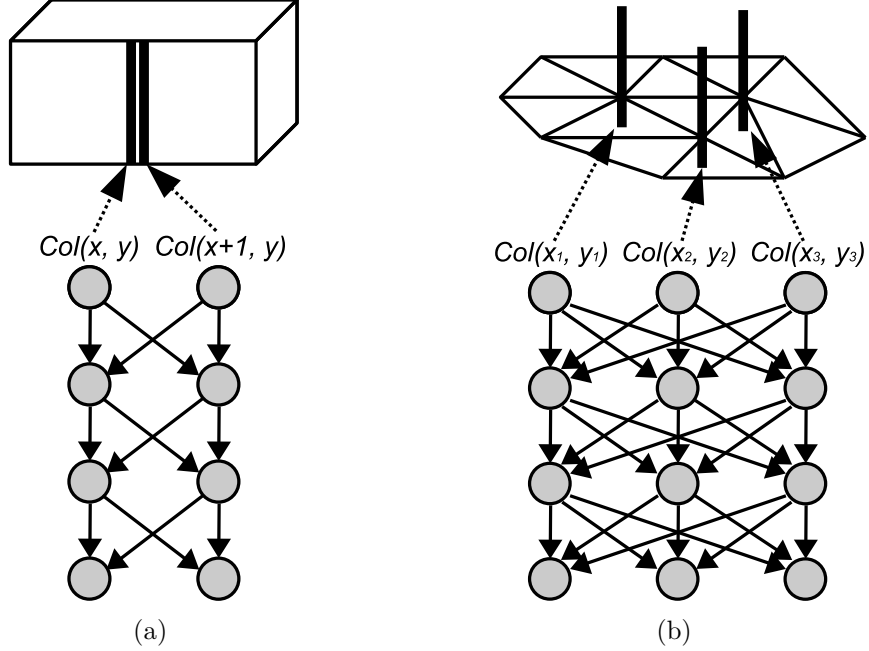
Figure 5.3: 3-D graph structures. (a) Unfolded plane-based graph. (b) Triangle mesh-based graph.

volumes is necessary to have a consistent retinal shape across scans and patients, and suppress eye movement artifacts. A reference surface for flattening was created by fitting a thin plate spline to surface 2 segmented in Section 5.1.1 excluding the subsurface close to the center of the optic disc cup to preserve the shape of the optic cup [19]. The center of the optic disc cup is the (x, y) location in which surface 1 has the lowest z-position. Based on the thin plate spline, the OCT volume was flattened by adjusting A-scans in the z-direction up and down. In addition, the retinal surfaces segmented in the original OCT volume were transformed into the flattened OCT volume. Fig. 5.2 shows the OCT volume and retinal surfaces flattened from the original OCT volume in Fig. 5.1.

5.1.3 Triangular mesh-based 3-D graph search

Compared with other segmentation methods such as level set methods [31,35,39], active shape models [11] and active appearance models [10], a 3-D graph search

approach has an advantage that it can detect an optimal surface with respect to a cost function. However, it is difficult to directly apply a conventional unfolded plane-based 3-D graph approach to the segmentation of 3-D retinal blood vessels (Fig. 5.3(a)). There are two reasons. One reason is that the unfolded plane-based graph search method requires the centerline of the retinal blood vessels to construct a graph. It may be imperfect to automatically extract the centerline using the 3-D thinning algorithm including the distance based-pruning process since information about short branch vessels might be lost [34]. The other reason is that it is difficult to construct a graph of bifurcations or crossovers of the retinal vessels. In order to overcome the limitations of the unfolded plane-based 3-D graph, we developed a triangle mesh-based 3-D graph search method in which columns were resampled using tri-linear interpolation along the average normal directions of surrounding triangles at the vertices of the surface of an initial vessel segmentation obtained by the marching cube algorithm (Fig. 5.3(b)) [28]. The adjacencies of the columns had been known from the triangle meshes of the initial vessel segmentation. The optimal vessel surface was detected by computing the minimum $s - t$ cut of the triangle mesh-based graph.

5.1.4 Triangular mesh generation of the initial 3-D retinal blood vessel model

The approximate retinal blood vessel model in 3-D was created using an OCT projection image and prior knowledge about the depth of retinal blood vessels. The $x-$ and $y-$positions of the retinal blood vessels were identified in the OCT projection image which was created by averaging in the z-direction the OCT subvolume between surfaces 2 and 3 segmented in Section 5.1.1 since the OCT projection image included high-contrast vessel shadows (Fig. 5.4). The vessel probability map of the OCT projection image was created using a supervised pixel classifier trained with features from multiscale Gaussian filters [33]. A binary vessel image was obtained by thresholding the vessel probability map. Additionally, using connected component analysis, small regions were removed since they are more likely to background noise.
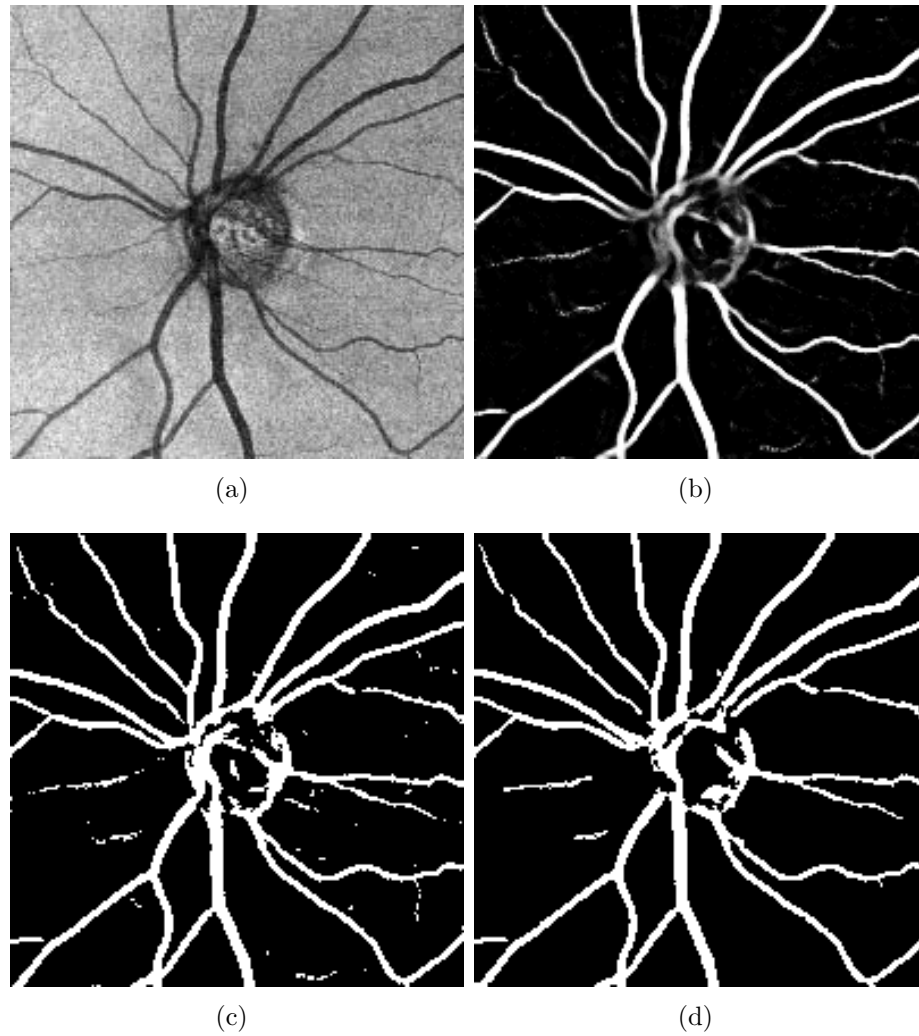
Figure 5.4: 2-D binary segmentation of the retinal blood vessels. (a) OCT projection image. (b) Vessel probability map. (c) Thresholded vessel probability map. (d) Final 2-D segmentation result of the retinal blood vessels in which small regions were deleted.

(a)

(b)

(c)

(d)
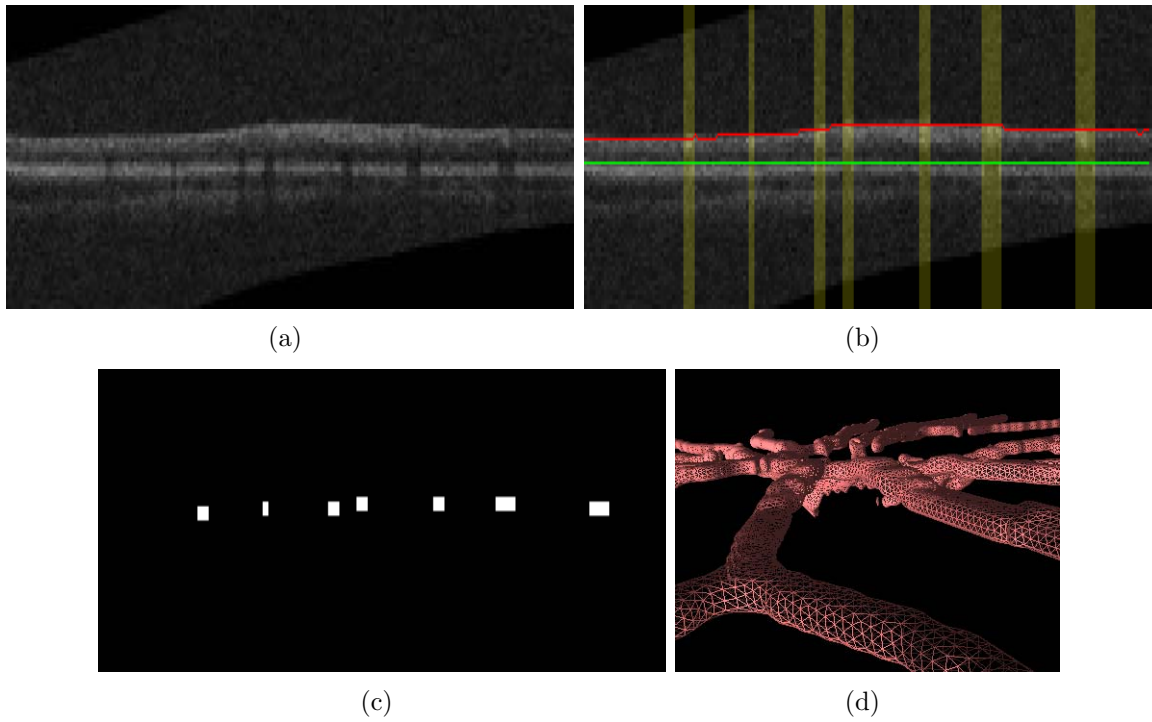
Figure 5.5: Triangular mesh generation of the initial 3-D retinal blood vessel model. (a) X-Z image of the isotropic OCT volume. (b) Image (a) overlapped with surfaces 1, 2 and the 2-D retinal blood vessel segmentation (yellow regions). (c) Approximate 3-D segmentation result of the retinal blood vessels. (d) 3-D rendering of the triangular mesh of the initial 3-D retinal blood vessel model.

According to Leitgeb's and Wehbe's papers [29, 44], the z-positions of the retinal blood vessels were identified in optical Doppler tomography (ODT) images that the retinal blood vessels were located right above vessel shadows in the OCT image. To detect isotropic retinal blood vessels, an isotropic OCT volume was created by subsampling in the z-direction the flattened OCT volume in which the voxel size is $30 \times 30 \times 2 \ \mu m$. Additionally, surfaces 1 and 2 in the flattened OCT volume in Section 5.1.2 were transformed into the isotropic OCT volume. The z-positions of the retinal blood vessels approximately corresponded to three middle voxels between surfaces 1 and 2. The approximate 3-D retinal blood vessels were detected by finding the intersection regions of the 2-D vessel segmentation and approximate z-positions of the vessels (Fig. 5.5). The triangular mesh of the initial 3-D retinal blood vessel model was built by applying the marching cube algorithm to the initial 3-D retinal blood vessel segmentation. Finally, the triangular mesh was smoothed by averaging adjacent vertices.

5.1.5 Final 3-D segmentation of the retinal blood vessels

Based on the initial 3-D retinal blood vessel model in Section 5.1.4, accurate 3-D segmentation of the retinal blood vessels was performed using a triangular mesh-based 3-D graph search method [28]. Columns of the graph were resampled using tri-linear interpolation along the average normal directions of surrounding triangles at the vertices of the triangular mesh of the initial 3-D retinal blood vessel model. The cost function for the graph search consisted of the inverted gradient magnitudes of the isotropic OCT volume and OCT projection image (Fig. 5.6). The gradient magnitudes of the OCT projection image were used to improve the gradient magnitudes of the sides of the retinal blood vessels. The optimal surfaces of the 3-D retinal blood vessels were detected by computing the minimum $s - t$ cut of the graph constructed from the cost function with a low-order polynomial time complexity. Finally, the surface of the segmented 3-D retinal blood vessel model was smoothed by averaging
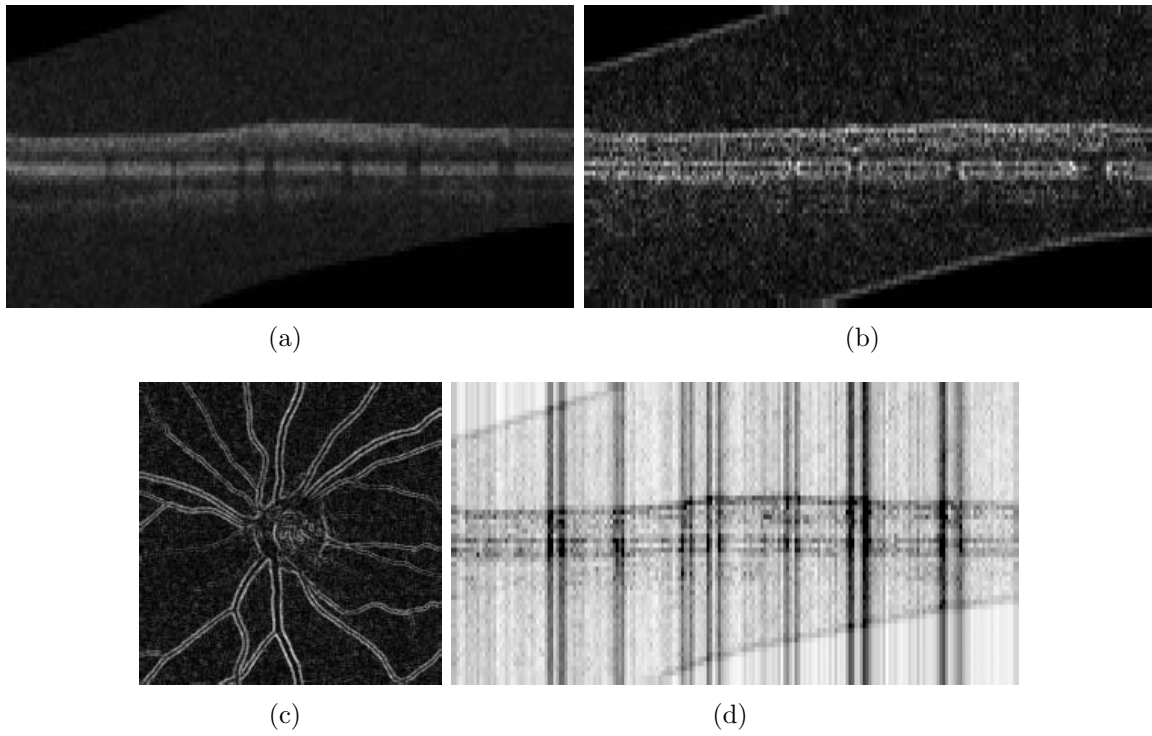
(a)

(b)

(c)

(d)

Figure 5.6: Cost function for the triangular mesh-based 3-D graph search. (a) Isotropic OCT volume. (b) Gradient magnitudes of (a). (c) Gradient magnitudes of the OCT projection image. (d) Final cost function which was inverted gradient magnitudes combined of (b) and (c).

adjacent vertices.

5.2 Experiments

5.2.1 Data

Thirty spectral-domain ONH-centered OCT scans were acquired from both the eyes of 15 glaucoma patients at the University of Iowa using Cirrus HD-OCT (Carl Zeiss Meditec, Inc., Dublin, CA, USA) machines. The dimension of each OCT scan was $200 \times 200 \times 1024$ voxels covering $6 \times 6 \times 2$ mm^3, the voxel size was $30 \times 30 \times 2$ μm, and the voxel depth was 8 bits in grayscale. The acquisition time of each OCT scan is 1.48 seconds. The Institutional Review Board of the University of Iowa approved the research protocol.

5.2.2 Validation

To validate the presented our 3-D segmentation method of the retinal blood vessels, our segmentation results were compared with markers which a retinal specialist put at the center of the retinal blood vessels in 10 randomly selected X-Z images for each isotropic OCT volume. Therefore, 300 X-Z images from 30 isotropic OCT volumes were used for validation. The unsigned error was calculated by measuring the closest Euclidean distance between a marker and all points of the centerline of our segmentation. The centerline was obtained by applying the 3-D thinning algorithm including the distance based-pruning process to the region surrounded by our triangular mesh-based segmentation [34].

5.3 Results

The mean unsigned error in the X-Y plane on 30 isotropic ONH-centered OCT scans was 1.326 ± 2.045 pixels (0.040 ± 0.061 mm), and that in the X-Y-Z plane was 3.375 ± 2.457 voxels (0.101 ± 0.074 mm). Figs. 5.7 and 5.8 show typical segmentation results of the 3-D retinal blood vessels.
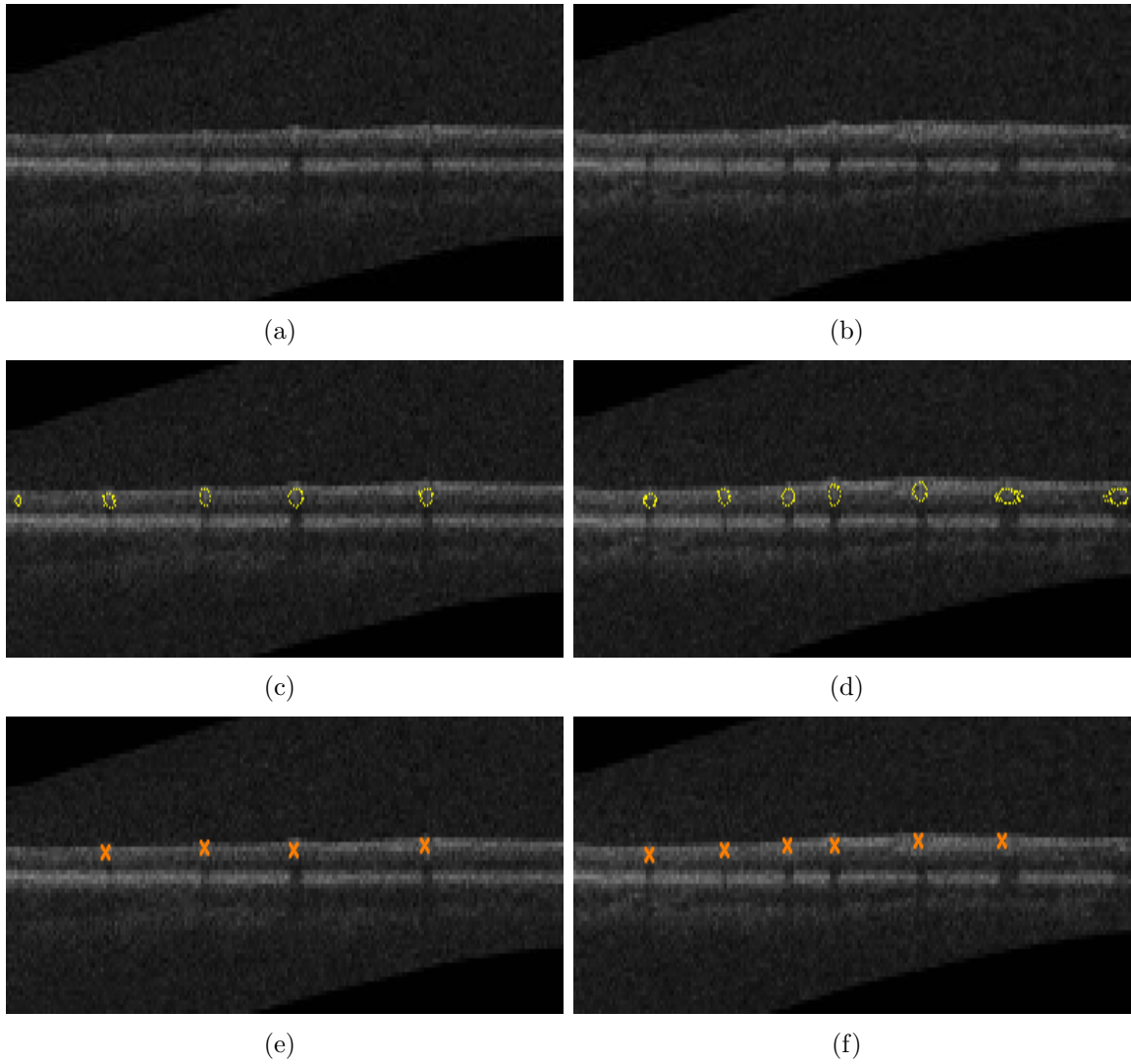
Figure 5.7: Segmentation results of the 3-D retinal blood vessels. (a) X-Z image of the isotropic OCT volume corresponding to the top dotted line in Fig. 5.8. (b) X-Z image of the isotropic OCT volume corresponding to the bottom dotted line in Fig. 5.8. (c) Image (a) overlapped with our segmentation result. (d) Image (b) overlapped with our segmentation result. (e) Image (a) overlapped with expert's markers. (f) Image (b) overlapped with expert's markers.
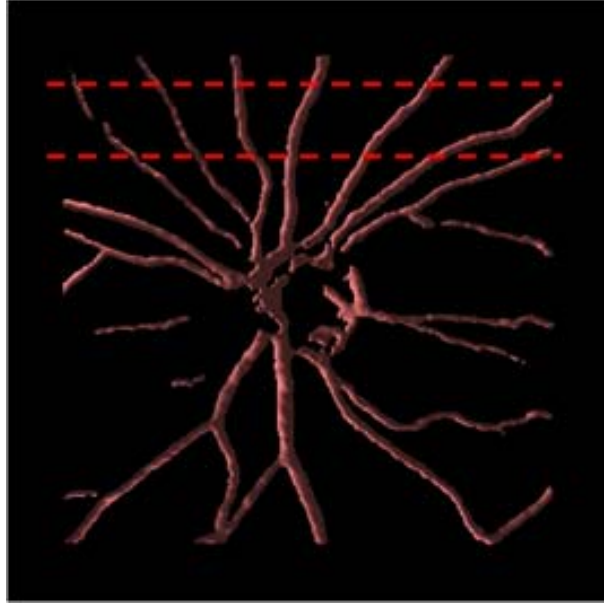
Figure 5.8: 3-D rendering of the retinal blood vessels segmented in Fig. 5.7.

5.4   Discussion

We have presented an automated 3-D segmentation method that can detect retinal blood vessels from spectral-domain ONH-centered OCT scans. This method utilizes a fast multiscale 3-D graph search to segment the retinal surfaces and a triangular mesh-based 3-D graph search to detect the retinal blood vessels. In general the method shows good performance. The average processing time of the reported method is 45 seconds (Windows XP Professional x64, Intel Core 2 Duo CPU @ 3.00 GHz, 4 GB of RAM). The segmentation of three retinal surfaces takes approximately 40 seconds, and the other processes including the retinal volume flattening, mesh generation of the initial vessel model and final segmentation of the retinal blood vessels require total 5 seconds. As the implementation was not optimized for speed, additional speed improvements can be expected.

From the mean unsigned errors in the X-Y and X-Y-Z planes reported in Section 5.3, the mean unsigned error in the z-axis was larger than those in the $x-$ and

$y-$axes. There are three main reasons of the unsigned errors. The first reason of the unsigned errors comes from the mis-segmented retinal blood vessels (the leftmost and rightmost vessels in Figs. 5.3(c) and (d), respectively). The second reason is caused by the segmentation of the retinal surfaces. Especially the top retinal surface (surface 1) has a variety of shapes including the large variation around the ONH in the z-direction. In addition, the segmentation results of the second and third retinal surface (surfaces 2, 3) are not accurate around the ONH since these two surfaces are obscure in the spectral-domain OCT scan as well as color fundus photographs. Therefore, some research about 2-D retinal vessel segmentation excluded the region around the ONH [18, 33]. Currently the edge-based cost functions for the 3-D graph searches were used to detect the retinal blood vessels. The addition of regional information to the cost functions could potentially increase the segmentation accuracy [19, 20]. The last reason comes from the 2-D binary segmentation of the retinal blood vessels in the OCT projection image. In Fig. 5.3(g), several thin blood vessels are disconnected, and some regions, which look like the retinal blood vessels, around the ONH are mis-segmented. To get a binary vessel segmentation in this study, a simple thresholding method was used. Piecewise thresholds obtained from local and global vessel features could be useful to improve the binary vessel segmentation [22]. In addition, more study on segmentation of the bifurcations and crossovers of the retinal vessels is required.

In Section 5.2.2, although it is more reasonable to compare our segmentation results with the vessel borders manually delineated by the retinal specialist, it is difficult to identify the vessel borders in isotropic OCT volumes (see Figs. 5.3(a), (b)). In the near future, more objective validation would be possible with optical Doppler tomography (ODT) scans registered onto the OCT scans.

CHAPTER 6
GENERAL DISCUSSION AND FUTURE DIRECTIONS

The methods developed for this thesis have a variety of potential applications. OCT registration could be possible using retinal surface segmentations from spectral-domain macular and ONH-centered OCT scans. In addition, more intraretinal layers in ONH-centered OCT scans could be segmented using the same technique used for the intraretinal layer segmentation method of macular OCT scans. Therefore, a large OCT volume including retinal surface segmentations could be obtained. Finally, an OCT viewer program was developed to visualize segmentation results of the retinal surfaces, optic disc and retinal blood vessels in the spectral-domain volumetric OCT scan.

6.1 Registration

OCT scanners such as Cirrus HD-OCT (Carl Zeiss Meditec, Inc., Dublin, CA, USA) have a limited lateral field of view which covers 6×6 mm of the retina. In order to get a larger view of the retina, OCT registration could be one solution. This section introduces an OCT registration method using segmented retinal surfaces of macular and ONH-centered OCT scans. The intraretinal layer thickness images of macular and ONH-centered OCT scans are registered by a rigid transformation. To calculate intraretinal layer thickness, the upper surface of the GCL and the lower surface of the RPE/BM is used. The upper surface of the GCL represents the outer surface of the retina, and the lower surface of the RPE/BM are used as a reference surface. After layer thickness registration, two OCT volumes are flatted based on the reference surface. Finally, these two OCT volumes are registered by a 3-D rigid transformation. Fig. 6.2 shows the OCT registration result. For fine adjustment, higher-order transformation could be applied to the registration result.
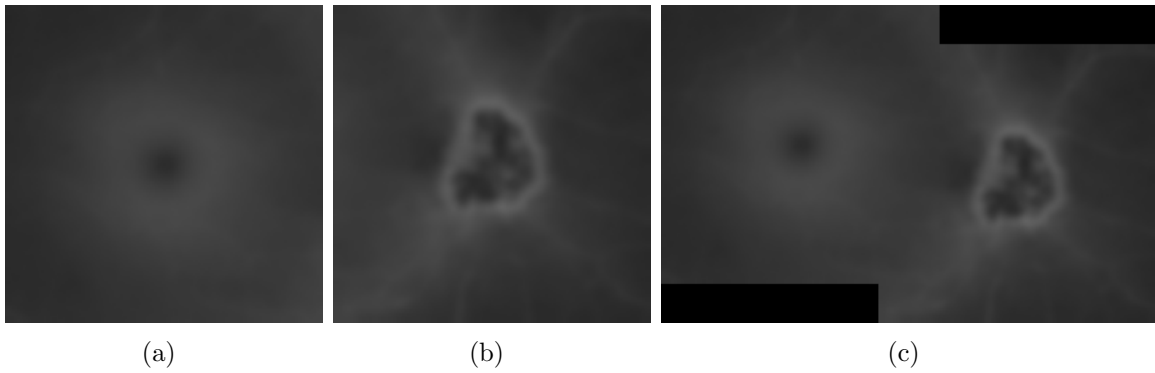
Figure 6.1: Registration of the intraretinal layer thickness. (a) Layer thickness image of the macular OCT scan. (b) Layer thickness image of the ONH-centered OCT scan. (c) Registration result.
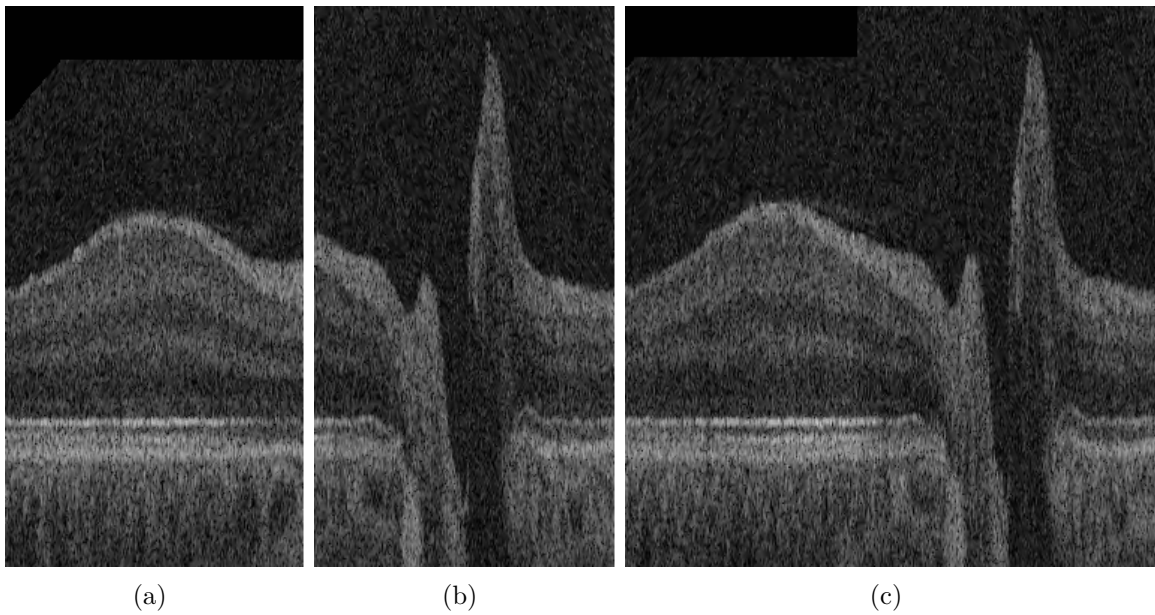

Figure 6.2: OCT registration result. (a) Flattened macular OCT scan. (b) Flattened ONH-centered OCT scan. (c) Registration result.
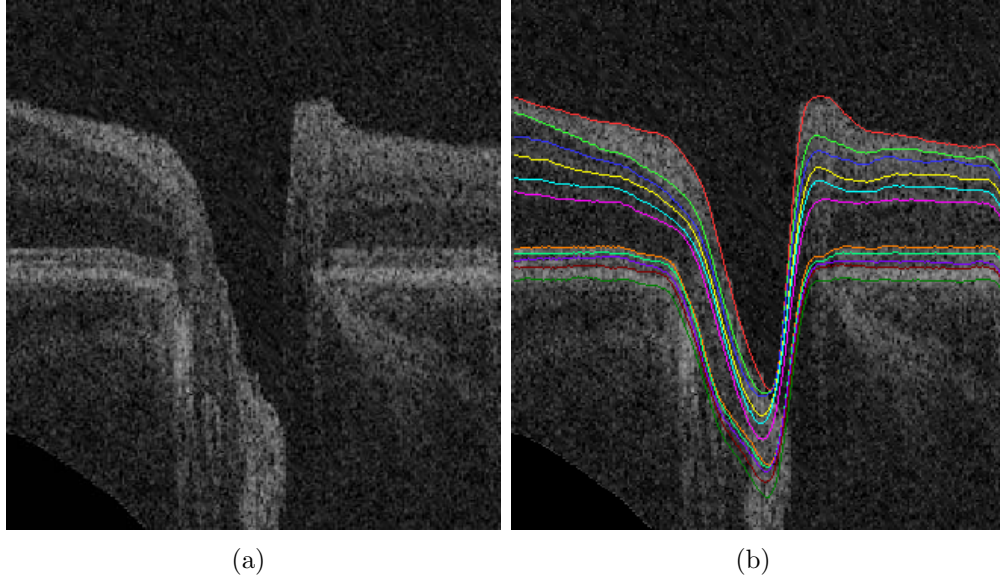
(a) (b)

Figure 6.3: Segmentation result of ten intraretinal layers in the ONH-centered OCT scan. (a) X-Z image of the flattened ONH-centered OCT scan. (b) Image (a) overlapped with the segmented retinal surfaces. The segmentation result around the ONH is not accurate since the intraretinal layers around the ONH are obscure.

6.2 Segmentation of ten intraretinal layers in ONH-centered OCT scans

The technique used for segmenting ten intraretinal layers in macular OCT scans is applicable to ONH-centered OCT scans. Fig 6.3 shows the segmentation result of ten intraretinal layers. Intraretinal layer segmentations in macular and ONH-centered OCT scans could be used as the initialization for segmentation of symptomatic exudate-associated derangements (SEADs) which are the abnormal dilation of the intraretinal layer thickness caused by choroidal neovascularization (CNV) and diabetic macular edema (DME) [19].

6.3 OCT viewer software

We developed an OCT viewer program to visualize cross-sectional images of the OCT volume, retinal surfaces, OCT projection images, optic discs and retinal blood vessels (Fig. 6.4). C++ was used for numerical calculation, and Microsoft foundation classes (MFC) was utilized for displaying 2-D images such as the cross-sectional OCT
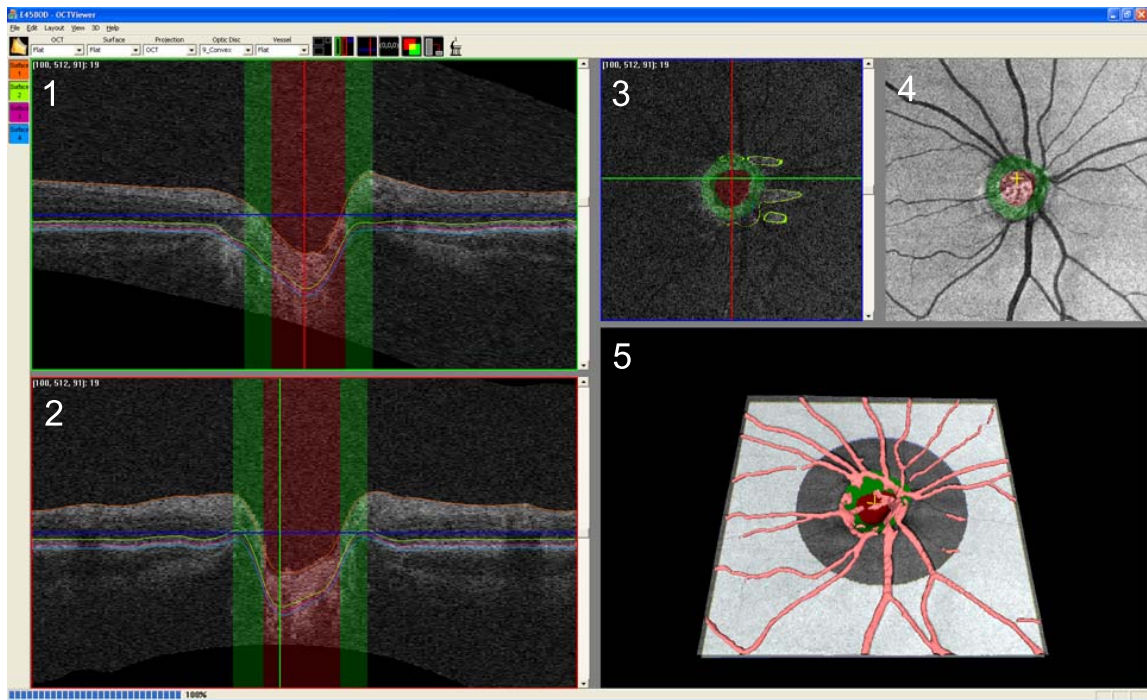
Figure 6.4: OCT viewer software. 1) X-Z image of the OCT volume. The optic disc cup is in red, and the neuroretinal rim is in green. The retinal surfaces are displayed on the X-Z image with various colors. 2) Y-Z image of the OCT volume. 3) X-Y image of the OCT volume. 4) OCT projection image. 5) 3-D rendering of the retinal surfaces with blending effects and retinal blood vessels.

images and OCT projection images. To visualize the retinal surfaces and blood vessels in 3-D, OpenGL was used.

CHAPTER 7
CONCLUSIONS

To summarize, first recall the specific aims for this thesis:

- **Aim 1:** Develop and validate a fast method that can automatically segment eleven retinal surfaces for ten intraretinal layers in the spectral-domain macular OCT scan.

- **Aim 2:** Develop and validate a shape-preserving method that can automatically segment the optic disc cup and neuroretinal rim in the spectral-domain OCT scan centered at the ONH.

- **Aim 3:** Develop and validate a method that can automatically segment the 3-D retinal blood vessels in the spectral-domain ONH-centered OCT scan.

Chapter 3 introduced a fast, accurate method which can automatically detect ten intraretinal layers using a multiscale 3-D graph search (Aim 1). The main contribution of the reported method is a fast processing performance by segmenting the retinal surfaces in the small subvolumes of the spectral-domain OCT scan. Chapter 4 described a classification-based optic disc segmentation method in the ONH-centered OCT scan using a multiscale 3-D graph search, contextual k-NN classifier and convex hull-based post-processing (Aim 2). A 3-D retinal blood vessel segmentation method from ONH-centered OCT scans using a triangular mesh-based 3-D graph search method was presented in Chapter 5 (Aim 3). In addition, Chapter 6 introduced potential future directions of these research.

In summary, this thesis has focused on the segmentations of the intraretinal layers, optic disc and retinal blood vessels in the spectral-domain OCT scan. The developed methods are expected to help analyze, diagnose and manage a variety of retinal diseases.

REFERENCES

[1] M. D. Abràmoff, W. L. M. Alward, E. C. Greenlee, L. Shuba, C. Y. Kim, J. H. Fingert, and Y. H. Kwon, "Automated segmentation of the optic disc from stereo color photographs using physiologically plausible features," *Investigative Ophthalmology & Visual Science*, vol. 48, no. 4, pp. 1665–1673, 2007.

[2] D. W. Aha and R. L. Bankert, "A comparative evaluation of sequential feature selection algorithms," in *Proceedings of the 5th International Workshop on Artificial Intelligence and Statistics*, 1995, pp. 1–7.

[3] S. Arya, D. M. Mount, N. S. Netanyahu, R. Silverman, and A. Wu, "An optimal algorithm for approximate nearest neighbor searching," *Journal of the ACM*, vol. 45, pp. 891–923, 1998.

[4] C. Gerth and R. J. Zawadzki and J. S. Werner and E. Héon, "Retinal microstructure in patients with efemp1 retinal dystrophy evaluated by fourier domain OCT," *Eye*, pp. 1–4, 2008.

[5] A. Can, H. Shen, J. N. Turner, H. L. Tanenbaum, and B. Roysam, "Rapid automated tracing and feature extraction from retinal fundus images using direct exploratory algorithms," *IEEE Transactions on Information Technology in Biomedicine*, vol. 3, no. 2, pp. 125–138, 1999.

[6] E. J. Carmona, M. Rincón, J. García-Feijoó, José, and M. M. de-la Casa, "Identification of the optic nerve head with genetic algorithms," *Artificial Intelligence in Medicine*, vol. 43, pp. 243–259, 2008.

[7] T. Chanwimaluang, G. Fan, and S. R. Fransen, "Hybrid retinal image registration," *IEEE Transactions on Information Technology in Biomedicine*, vol. 10, no. 1, pp. 126–142, 2006.

[8] S. Chiba and N. Tanno, "Backscattering optical heterodyne tomography," in *Proceedings of the 14th Laser Sensing Symposium*, 1991.

[9] R. Chrástek, M. Wolf, K. Donath, H. Niemann, D. Paulus, T. Hothorn, B. Lausen, R. Lámmer, C. Mardin, and G. Michelson, "Automated segmentation of the optic nerve head for diagnosis of glaucoma," *Medical Image Analysis*, vol. 9, pp. 297–314, 2005.

[10] T. F. Cootes, G. J. Edwards, and C. J. Taylor, "Active appearance models," *IEEE Transactions on Pattern Analysis and Machine Intelligence*, vol. 23, no. 6, pp. 681–685, 2001.

[11] T. F. Cootes, C. J. Taylor, D. H. Cooper, and J. Graham, "Active shape models – their training and application," *Computer Vision and Image Understanding*, vol. 61, no. 1, pp. 38–59, 1995.

[12] Early Treatment Diabetic Retinopathy Study research group, "Early photocoagulation for diabetic retinopathy. ETDRS report number 9," *Ophthalmology*, vol. 98, no. 5, pp. 766–785, 1991.

[13] T. Eom, J. Sung, C. Kee, D. Ko, J. Lee, and E. Choi, "Wavelength-tunable broadband frequency-domain OCT source based on spatially filtered sub-10-fs pulsed laser," *IEEE Photonics Technology Letters*, vol. 20, no. 12, pp. 994–996, 2008.

[14] A. F. Fercher, C. K. Hitzenberger, C. K. Kamp, and S. Y. El-Zayat, "Measurement of intraocular distances by backscattering spectral interferometry," *Optics Communications*, vol. 117, no. 1, pp. 43–48, 1995.

[15] A. F. Fercher, K. Mengedoht, and W. Werner, "Eye length measurement by interferometry with partially coherent light," *Optics Letters*, vol. 13, no. 3, pp. 186–188, 1988.

[16] D. C. Fernández, H. M. Salinas, and C. A. Puliafito, "Automated detection of retinal layer structures on optical coherence tomography images," *Optics Express*, vol. 13, no. 25, pp. 10 200–10 216, 2005.

[17] A. R. Fuller, R. J. Zawadzki, S. Choi, D. F. Wiley, J. S. Werner, and B. Hamann, "Segmentation of three-dimensional retinal image data," *IEEE Transactions on Visualization and Computer Graphics*, vol. 13, no. 6, pp. 1719–1726, 2007.

[18] L. Gang, O. Chutatape, and S. M. Krishnan, "Detection and measurement of retinal vessels in fundus images using amplitude modified second-order gaussian filter," *IEEE Transactions on Biomedical Engineering*, vol. 49, no. 2, pp. 168–172, 2002.

[19] M. K. Garvin, *Automated 3-D segmentation and analysis of retinal optical coherence tomography images*. PhD thesis, The University of Iowa, 2008.

[20] M. K. Garvin, M. D. Abràmoff, R. Kardon, S. R. Russell, X. Wu, and M. Sonka, "Intraretinal layer segmentation of macular optical coherence tomography images using optimal 3-D graph search," *IEEE Transactions on Medical Imaging*, vol. accepted, 2008.

[21] T. H. Goldsmith, "Optimization, constraint, and history in the evolution of eyes," *The Quarterly Review of Biology*, vol. 65, no. 3, p. 281, 1990.

[22] A. Hoover, V. Kouznetsova, and M. Goldbaum, "Locating blood vessels in retinal images by piecewise threshold probing of a matched filter response," *IEEE Transactions on Medical Imaging*, vol. 19, no. 3, pp. 203–210, 2000.

[23] D. Huang, E. A. Swanson, C. P. Lin, J. Schuman, W. G. Stinson, W. Chang, M. R. Hee, T. Flotte, K. Gregory, C. A. Puliafito, and et al., "Optical coherence tomography," *Science*, vol. 254, no. 5035, pp. 1178–1181, 1991.

[24] D. Klonoff, "An economic analysis of interventions for diabetes." *Diabetes Care*, vol. 23, no. 3, pp. 390–404, 2000.

[25] H. Kolb, "How the retina works," *American Scientist*, vol. 91, no. 1, pp. 28–35, 2003.

[26] Y. Kwon, M. Adix, M. Zimmerman, S. Piette, E. Greenlee, L. Alward, and M. D. Abràmoff, "Variance due to observer, repeat imaging, and fundus camera type on cup-to-disc ratio estimates by stereo planimetry," *Journal of Glaucoma*, vol. in press, 2009.

[27] K. Lee, M. Niemeijer, M. K. Garvin, Y. H. Kwon, M. Sonka, and M. D. Abràmoff, "3-D segmentation of the rim and cup in spectral-domain optical coherence tomography volumes of the optic nerve head," in *Proceedings of the SPIE*, vol. 7262, 2009.

[28] K. Lee, Y. Yin, A. Wahle, M. E. Olszewski, and M. Sonka, "3-D segmentation and quantitative analysis of inner and outer walls of thrombotic abdominal aortic aneurysms," in *Proceedings of the SPIE*, vol. 6916, 2008, pp. 691 626–691 626.9.

[29] R. A. Leitgeb, L. Schmetterer, W. Drexler, and A. F. Fercher, "Real-time assessment of retinal blood flow with ultrafast acquisition by color Doppler Fourier domain optical coherence tomography," *Optics Express*, vol. 11, no. 23, pp. 3116–3121, 2003.

[30] K. Li, X. Wu, D. Z. Chen, and M. Sonka, "Optimal surface segmentation in volumetric images - a graph-theoretic approach," *IEEE Transactions on Pattern Analysis and Machine Intelligence*, vol. 28, no. 1, pp. 119–134, 2006.

[31] R. Malladi, J. A. Sethian, and B. C. Vemuri, "Shape modeling with front propagation: A level set approach," *IEEE Transactions on Pattern Analysis and Machine Intelligence*, vol. 17, no. 2, pp. 158–175, 1995.

[32] National Eye Institute, "Diabetic retinopathy," 2006. [Online]. Available: http://www.nei.nih.gov

[33] M. Niemeijer, M. K. Garvin, B. van Ginneken, M. Sonka, and M. D. Abràmoff, "Vessel segmentation in 3D spectral OCT scans of the retina," in *Proceedings of the SPIE*, vol. 6914, 2008, p. 69141.

[34] K. Palagyi, E. Sorantin, A. Kuba, C. Halmai, B. Erdohelyi, E. Sorantin, and K. Hausegger, "A sequential 3D thinning algorithm and its medical applications," in *Proceedings of the 17th Int'l Conf. Information Processing in Medical Imaging (IPMI)*, 2001, pp. 409–415.

[35] N. Paragios and R. Deriche, "Geodesic active regions and level set methods for supervised texture segmentation," *International Journal of Computer Vision*, vol. 46, no. 3, pp. 223–247, 2002.

[36] R. Perfetti, E. Ricci, D. Casali, and G. Costantini, "Cellular neural networks with virtual template expansion for retinal vessel segmentation," *IEEE transactions on Circuits and Systems*, vol. 54, no. 2, pp. 141–145, 2007.

[37] H. A. Quigley, "Number of people with glaucoma worldwide," *British Journal of Ophthalmology*, vol. 80, pp. 389–393, 1996.

[38] J. M. Schmitt, "Optical coherence tomography (OCT): A review," *IEEE Selected Topics in Quantum Electronics*, vol. 5, no. 4, pp. 1205–1215, 1999.

[39] J. A. Sethian, *Level Set Methods and Fast Marching Methods.* New York, NY: Cambridge University Press, 1999.

[40] J. Staal, M. D. Abrámoff, M. Niemeijer, M. A. Viergever, and B. van Ginneken, "Ridge-based vessel segmentation in color images of the retina," *IEEE Transactions on Medical Imaging*, vol. 23, no. 4, pp. 501–509, 2004.

[41] The Washington University School of Medicine, "Neuroscience tutorial," 1997. [Online]. Available: http://thalamus.wustl.edu

[42] J. M. Tielsch, A. Sommer, J. Katz, R. M. Royall, H. A. Quigley, and J. Javitt, "Racial variations in the prevalence of primary open-angle glaucoma: the Baltimore eye survey," *The Journal Of the American Medical Association*, vol. 266, no. 3, pp. 369–374, 1991.

[43] U.S. National Library of Medicine and National Institutes of Health, "Diabetic retinopathy," 2008. [Online]. Available: http://www.nlm.nih.gov

[44] H. Wehbe, M. Ruggeri, S. Jiao, G. Gregori, C. A. Puliafito, and W. Zhao, "Automatic retinal blood flow calculation using spectral domain optical coherence tomography," *Optics Express*, vol. 15, no. 23, pp. 15 193–15 206, 2007.

[45] X. Wu and D. Z. Chen, "Optimal net surface problems with applications," in *Proceedings of the 29th International Colloquium on Automata, Languages, and Programming (ICALP)*, vol. 2380, 2002, pp. 1029–1042.

[46] J. Xu, H. Ishikawa, G. Wollstein, R. A. Bilonick, K. R. Sung, L. Kagemann, K. A. Townsend, and J. S. Schuman, "Automated assessment of the optic nerve head on stereo disc photographs," *Investigative Ophthalmology & Visual Science*, vol. 49, no. 6, pp. 2512–2517, 2008.

[47] F. Zana and J.-C. Klein, "Segmentation of vessel-like patterns using mathematical morphology and curvature evaluation," *IEEE Transactions on Image Processing*, vol. 10, no. 7, pp. 1010–1019, 2001.

[48] K. H. Zou, S. K. Warfield, A. Bharatha, C. M. C. Tempany, M. R. Kaus, S. J. Haker, W. M. Wells, F. A. Jolesz, and R. Kikinis, "Statistical validation of image segmentation quality based on a spatial overlap index," *Academic Radiology*, vol. 11, no. 2, pp. 178–189, 2004.